Chapter 11: Inverse Methods using KF, EKF, EIF, PF, and LS Techniques for Detection, Localization, and Parameter Estimation

Chapter details

Chapter DOI:

https://doi.org/10.4322/978-65-86503-71-5.c11

Chapter suggested citation / reference style:

Myers, Michael R., Jorge, Ariosto B. (2022). "Inverse Methods using KF, EKF, EIF, PF, and LS Techniques for Detection, Localization, and Parameter Estimation". *In* Jorge, Ariosto B., et al. (Eds.) *Model-Based and Signal-Based Inverse Methods*, Vol. I, UnB, Brasilia, DF, Brazil, pp. 382–442. Book series in Discrete Models, Inverse Methods, & Uncertainty Modeling in Structural Integrity.

P.S.: DOI may be included at the end of citation, for completeness.

Book details

Book: Model-based and Signal-Based Inverse Methods

Edited by: Jorge, Ariosto B., Anflor, Carla T. M., Gomes, Guilherme F., & Carneiro, Sergio H. S.

Volume I of Book Series in:

Discrete Models, Inverse Methods, & Uncertainty Modeling in Structural Integrity

Published by: UnB City: Brasilia, DF, Brazil Year: 2022

DOI: https://doi.org/10.4322/978-65-86503-71-5

Inverse Methods using KF, EKF, EIF, PF, and LS Techniques for Detection, Localization, and Parameter Estimation

Michael Richard Myers[1*], Ariosto Bretanha Jorge[2]

[1*]Senior Systems Modeling & Simulation Engineer, Axiom Space, Inc., Houston, Texas, USA.
E-mail: mike.myers@funkandmyers.com
[2]Post-Graduate Program - Integrity of Engineering Materials, University of Brasilia, Brazil.
E-mail: ariosto.b.jorge@gmail.com

*Corresponding author.

Abstract

This chapter presents some fundamental concepts for detection, localization, and parameter estimation using Kalman filter, extended Kalman filter, extended information filter, particle filter, and least squares. These techniques can be used to characterize singularities, discontinuities, material properties, boundary conditions, loading, damage, structural changes, etc. Unfortunately, directly characterizing parameters of interest such as structural damage and concentrated heating sources is often difficult or not possible with current sensors. Other quantities can be measured and the parameters of interest can be estimated using an inverse method. Several types of static and dynamic loads and the structural deterioration process can cause different types of structural damage. Parameter estimation addresses the problem of estimating quantities that are not directly observable and can be inferred from sensor data. Sensors carry only partial information and their measurements are corrupted by noise. Parameter estimation seeks to recover state variables from the sensor data. Probabilistic parameter estimation algorithms compute belief distributions over possible world states.

Keywords

detection, localization, paramter estimation, characterization, structural damage, heating source, material properties, Kalman filter, extended Kalman filter, particle filter, least squares, information filter.

1 Introduction

It is increasingly essential that a structure or equipment not fail. When considering the particular case of an aircraft wing, where failure can be catastrophic, it is possible to see the importance of maintaining structural integrity. All aircraft receive maintenance during its life, where the frequency and type of maintenance depend on the type of aircraft and the cycle (takeoff - landing) or flight hours. But some points of the aircraft are difficult to access, if not impossible, without damaging the structure. In order to monitor these points, it was thought the inclusion of sensors during manufacture, that during the same maintenance in a hangar, a window would have access to the communication of sensors, with some equipment for data collection. These data provided by sensors, with the analysis made by the present method in a station of data collection, indicate the presence or absence of damage to the monitored region of the structure. Structural damage estimates could be compared between two independent objective functions such as mean stress and octahedral stress. A pareto front could be used to find the best match.

Characterizing concentrated heating sources is another engineering challenge. For example, knowledge of where air flowing across a body transitions from laminar flow to turbulent flow (Figure 1) can provide numerous

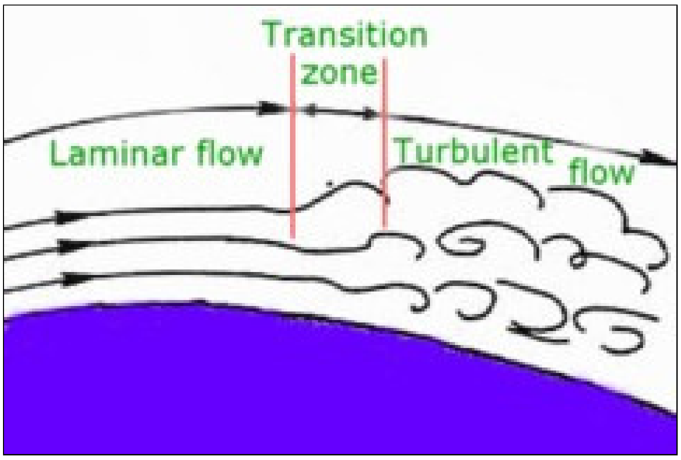

Figure 1: Flow regimes Recreational Aviation Australia [2010].

benefits to air vehicle design, thermal protection system design, and air vehicle in-flight control Reed et al. [1997]. Of particular interest is the transition region for hypersonic vehicles (Mach 5+). At the transition between laminar and turbulent flow, a change in body-surface temperature has been measured for hypersonic conditions Horvath et al. [2002], Schneider [1999, 2004], Berger et al. [2009] and is illustrated in Figure 2. Thus, a measurement system is envisioned that leverages the hypersonic body-surface heating profile to locate the boundary layer transition region.

Unfortunately, directly characterizing structural damage and concentrated heating sources is often difficult or not possible with current sensors. Other quantities can be measured and the parameters of interest can be estimated using an inverse method. Several types of static and dynamic loads and the structural deterioration process can cause different types of structural damage. The damage can be characterized by a change in the structure, such as the presence of holes and cracks. The knowledge of the change in the material properties corresponding to the damage depends on the type of material and structural configurations. The proper assessment of the damage in a structure can be useful to infer its remaining service life. The assessment of the structural damage can be performed through a comparison between measured and simulated data. To provide the simulated data, a numerical code is required, in which a direct model of the problem is consistently used by an inverse problem algorithm. For the direct problem, a model is required to obtain the information on the distribution of the quantity of interest throughout the structure, given the boundary conditions and the presence of the damage. For the inverse problem, a model is required for the procedure of locating the damage in the structure given some (partial) information on the quantity of interest at some particular locations (e.g. where some sensors are placed).

The presence of damage may induce rapid changes in the field variable of the problem and even discontinuities in the governing equation in the domain. Classical calculus-based optimization methods require evaluation of derivatives of the objective function, which may not be possible to be obtained, or may be numerically obtained, with unacceptable inaccuracy. These problems can also have several local minima (multiple solutions), and thus a global optimization method is a better choice for the numerical solution Stavroulakis and Antes [1998], Engelhardt et al. [2006].

Numerical methods, such as the boundary element method or the finite element method can be used for modelling the direct problem. The damage detection problem can be considered as a problem of system identification or an inverse problem. The inverse problem of identifying the presence, location and size of damage, such as cracks and holes, in a plate structure can be modelled using optimization and parameter identification techniques. The remainder of this chapter focuses on inverse methods using finite element method and the annex focuses on inverse methods using boundary element method Vieira et al. [2011].

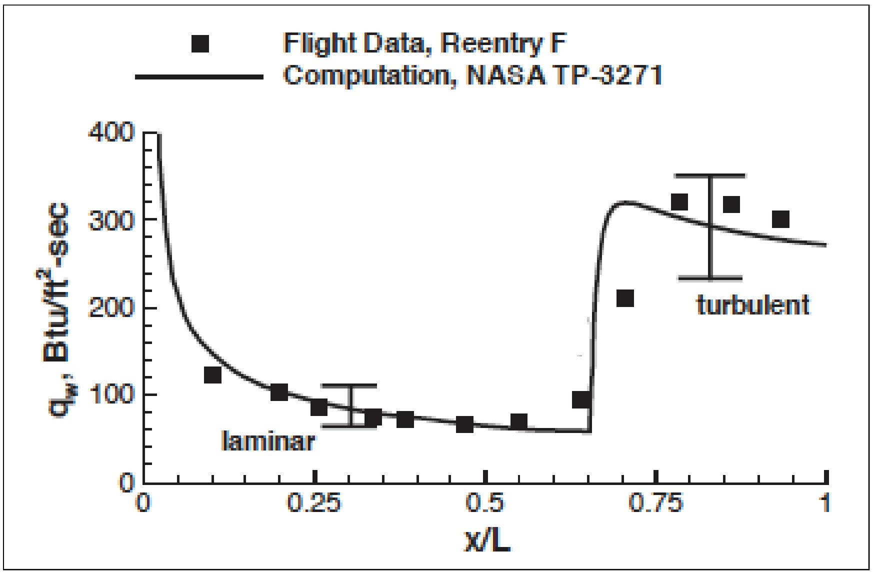

Figure 2: Heating profile on a ballistic RV, peak Mach=20 Schneider [2004].

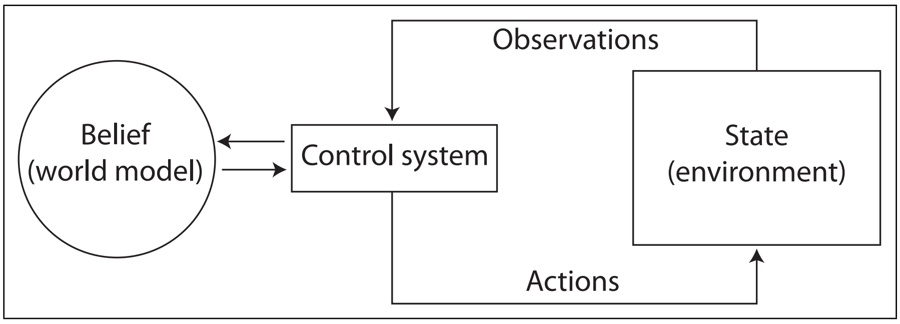

Figure 3: Object-environment interaction.

2 Detection, localization, and parameter estimation

Figure 3 illustrates the conceptual interaction of an object with its environment. The environment is a dynamic system that possesses an internal state. It is convenient to think of the state as the collection of all the object's aspects and its environment that can affect the future. Certain state variables can change over time such as the object's speed, acceleration, temperature, and location. Other state variables tend to remain static, such as the location of the ground or the earth. There are endless possibilities for potential state variables. The first challenge is to determine which of the potential state variables are important and need to be included in the problem. Throughout this chapter, state will be denoted X and the specific variables included in the state will depend upon the context. The state at time t will be denoted X_t. Time is considered discrete, that is, all interesting events take place at discrete time steps $t = 0, 1, 2, \ldots$.

There are two fundamental types of interactions between an object and its environment: The object can influence the state of its environment through its control system, and it can gather information about the state through its sensors. Control actions include moving control surfaces and applying force to accelerate or decelerate the object. Sensors are noisy and many parameters cannot be measured directly. As a consequence, the object maintains an internal belief with regards to its state. The distinction between measurement and control is crucial. While measurements over time tend to increase the object's knowledge, motion and control inputs tend to induce a loss of knowledge due to the inherent noise in control actuation and the stochasticity of the environment.

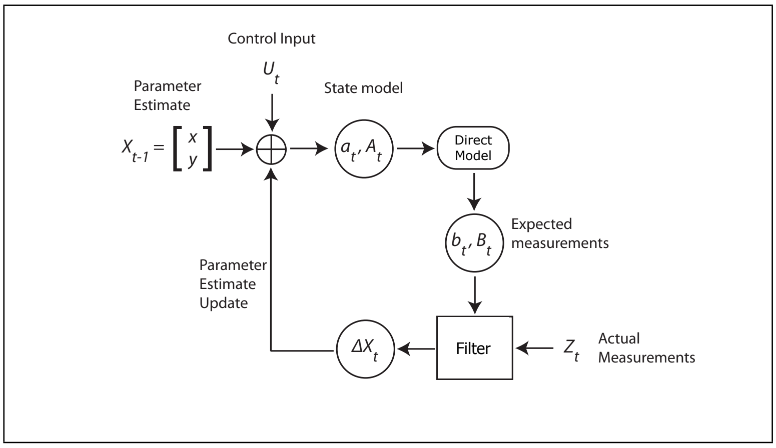

Figure 4: Parameter estimate update process using an inverse method and a direct model.

Parameter estimation addresses the problem of estimating quantities that are not directly observable but that can be inferred from sensor data. Sensors carry only partial information and their measurements are corrupted by noise. Parameter estimation seeks to recover state variables from the sensor data. Probabilistic parameter estimation algorithms compute belief distributions over possible world states. A state X_t is called complete if it is the best predictor of the future. Completeness entails that knowledge of past states, measurements, and control inputs carry no additional information that would help us predict the future more accurately. In practice, it is impossible to specify a complete state for any realistic singularity or discontinuity situation. A complete state includes not only aspects of the object itself and of the environment immediately surrounding the object being studied but also the environment away from the object that may affect its future. Some of these elements are hard to obtain and therefore practical implementations single out a small subset of all state variables.

The Markov assumption postulates that past and future data are independent if one knows the current state X_t. Unmodeled environment dynamics, inaccuracies in probabilistic models, and approximation errors induce violations of the Markov assumption. In principle, many of these variables can be included in the state, however, incomplete state representations are often preferable to more complete ones to reduce the computational complexity of the filter algorithm. It is advisable to exercise care when defining the state X_t so that the effect of unmodeled state variables has close to random effects.

Figure 4 illustrates the parameter estimate update process for an inverse method and a direct model. The estimated state is $X_t = [x_s, y_s]^T$ where x_s and y_s represent the estimated parameters of interest at time t. The parameters of interest (state) may be the location and size of structural damage or concentrated heating source.

3 Methods

This section details some inverse methods that have proven useful for estimating state variables that cannot be directly observed.

3.1 Kalman Filter

The Kalman filter was developed by R. E. Kalman in 1960 to solve the model of space state of Wierner, recursively. Combining the filter with the advances in digital computing, the technique had a strong application in automation and assisted navigation. The Kalman filter, was originally developed for discrete linear systems and have white Gaussian noise. What does not occur in real systems, but may, in some regions, be approximated to linear, extending its application. But for the Kalman filter is able to estimate the state, it is necessary that the process is observable. This filter is the original Kalman filter and provided the basis for the development of derivatives, the extended Kalman filter, and many hybrid filters.

The Kalman filter is a member of a family of recursive state estimators collectively called Gaussian filters.

Table 1: Kalman filter algorithm.

Step	Operation
1	$\overline{X}_t = A_t X_{t-1} + B_t X_t$
2	$\overline{\Sigma}_t = A_t \Sigma_{t-1} A_t^T + Q_t$
3	$K_t = \overline{\Sigma}_t C_t^T (C_t \overline{\Sigma}_t C_t^T + R_t)^{-1}$
4	$X_t = \overline{X}_t + K_t(Z_t - C_t \overline{X}_t)$
5	$\Sigma_t = (I - K_t C_t)\overline{\Sigma}_t$
6	Return to step 1 for next time step

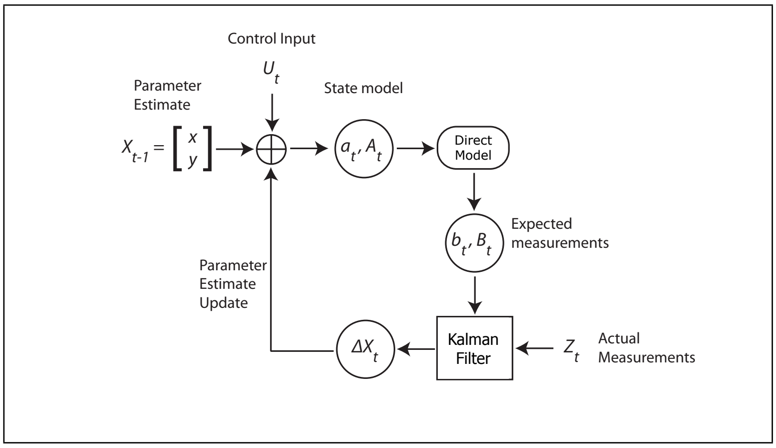

Figure 5: Parameter estimate update process using the Kalman filter and a direct model.

Historically, Gaussian filters constitute the earliest tractable implementations of the Bayes filter for continuous spaces Thrun et al. [2006]. Kalman filters construct a framework of predicting the state based on an input to the system and correcting the predicted state based on sensor observations. Kalman filters were invented by Swerling (1958) and Kalman (1960) as a technique for filtering and prediction in linear Gaussian systems Thrun et al. [2006]. Kalman filters assume that all continuous random variables possess probability density functions (PDFs). A common density function is that of the one-dimensional normal distribution with mean μ and variance σ^2. The PDF of a normal distribution is given by the following Gaussian function:

$$p(x) = (2\pi\sigma^2)^{-\frac{1}{2}} \exp\left\{-\frac{1}{2}\frac{(x-\mu)^2}{\sigma^2}\right\} \tag{1}$$

Normal distributions play a major role in Kalman filters and are abbreviated as $N(\mu, \sigma^2)$ which specifies mean of the random variable and its variance. The normal distribution in equation 1 assumes that x is a scalar value. All Gaussian filters share the basic premise that beliefs are multivariate normal distributions. The PDF of a multivariate normal distribution is given by the following Gaussian function:

$$p(X) = \det(2\pi\Sigma)^{-\frac{1}{2}} \exp -\frac{1}{2}(X-\mu)^T \Sigma^{-1}(X-\mu) \tag{2}$$

Where X is a multivariate vector, μ is the mean vector, Σ is a positive semidefinite and symmetric matrix called the covariance matrix.

The Kalman filter consists of two phases, the phase prediction and phase correction. After the initial estimate, the Kalman filter begins one update cycle of the two phases until convergence of the state, ie, the state predicted corresponds to the state that generated the measurement. Figure 5 illustrates the process cycle of Kalman filter and Table 1 contains the full Kalman filter algorithm.

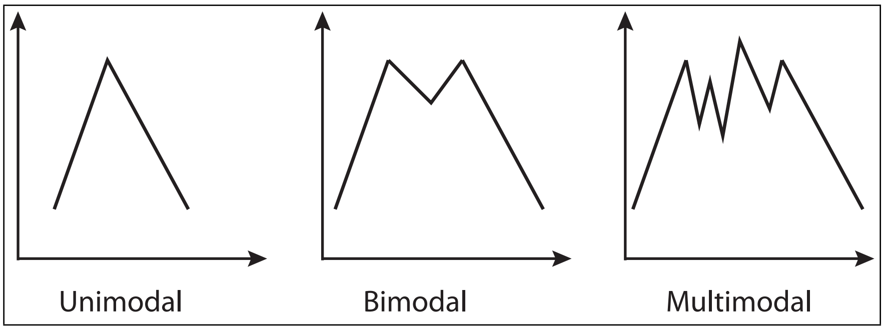

Figure 6: Unimodal illustration.

3.2 Extended Kalman Filter

The extended Kalman filter linearizes nonlinear Gaussian systems. Kalman filters implement belief computation for continuous states with all disturbances additive and Gaussian with zero mean.

$$X_t = a(U_t, X_{t-1}) + \epsilon_t, \quad \epsilon_t \sim N(0, Q_t) \tag{3}$$

$$Z_t = b(X_t) + \delta_t, \quad \delta_t \sim N(0, R_t) \tag{4}$$

Where a and b are nonlinear functions, U_t is the input, X_t is the state, Z_t is the observation, and $\epsilon_t \sim N(0, Q_t)$ and $\delta_t \sim N(0, R_t)$ represent Gaussian random disturbances with zero mean and the specified covariance. a represents the state transition function and its purpose is to predict the current state $\overline{X}_t$, based on the previous state X_{t-1} and the current control input U_t. For a hypersonic vehicle, the control input to the extended Kalman filter could be the pilot's flight control commands (e.g., throttle, attitude controls, etc.) and sensor data (e.g., angle of attack, altitude, etc.). b represents the measurement transition function and are the expected measurements based on the current state X_t. ϵ_t is a Gaussian random variable that models the uncertainty introduced by the state transition function and δ_t describes the measurement noise.

Kalman filters assume a unimodal approximation to the true belief. A function is unimodal if for some value m (the mode), it is monotonically increasing for $x \leq m$ and monotonically decreasing for $x \geq m$. In that case, the maximum value of $f(x)$ is $f(m)$ and there are no other local maxima (Figure 6).

The Kalman filter assumes linear state and measurement models. Unfortunately, state transitions and measurements are rarely linear in practice. The extended Kalman filter relaxes this linear assumption by approximating the nonlinear state and measurement models with a first order Taylor expansion linear model (Figure 7). Instead of passing the Gaussian through the nonlinear function g, it is passed through a linear approximation of g. The linear function is tangent to g at the mean of the original Gaussian. The resulting Gaussian is shown as the dashed line in the upper left graph. The linearization incurs an approximation error, as indicated by the mismatch between the linearized Gaussian (dashed) and the Gaussian computed from the highly accurate but expensive Monte-Carlo estimate (solid).

The extended Kalman filter is computationally quite efficient (Table 2). It is polynomial in measurement dimensionality k and state dimensionality $n : O(k^{2.4}+n^2)$ Thrun et al. [2006]. The input to the extended Kalman filter is the belief at time $t-1$ represented by X_{t-1} and Σ_{t-1}. In step 1, the predicted state $\overline{X}_t$ is computed using the state transition function $a(U_t, X_{t-1})$ and the control input. The uncertainty estimate $\overline{\Sigma}_t$ grows in step 2 by incorporating the state model Jacobian A_t, the state model covariance Q_t, and the uncertainty from the previous time step Σ_{t-1}. The Kalman gain is computed in step 3 by leveraging the predicted covariance $\overline{\Sigma}_t$, the measurement transition Jacobian B_t which contain the derivatives of the measurements with respect to the state variables, and the measurement covariance matrix R_t. The Kalman gain specifies the degree that the measurement update Z_t is incorporated into the new state estimate X_t. The output is the belief at time t, represented by X_t and Σ_t, which are computed in steps 4 and 5 where the Kalman gain is incorporated. The measurement update corrects the predicted state $\overline{X}_t$ and shrinks the uncertainty. The filter represents the belief at time t by the state X_t and the covariance Σ_t.

Figure 8 illustrates the parameter estimate update process for an extended Kalman filter and a direct model. The estimated state is $X_t = [x_s, y_s]^T$ where x_s and y_s represent the estimated parameters of interest at time t.

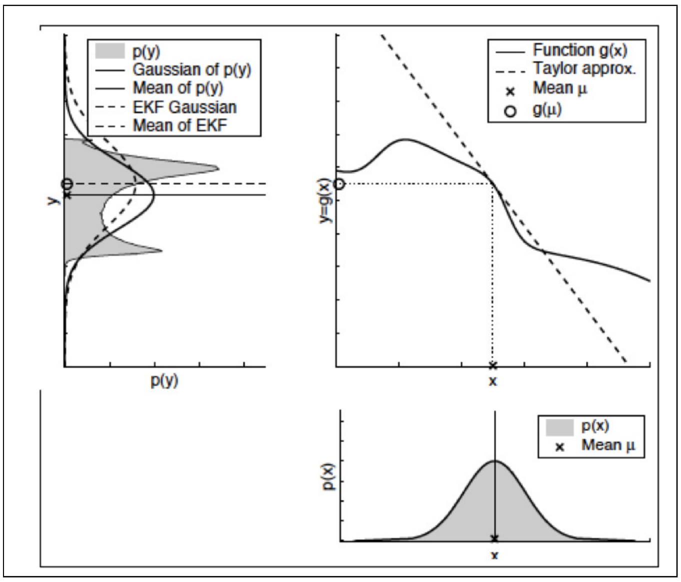

Figure 7: Illustration of linearization applied by the extended Kalman filter Thrun et al. [2006].

Table 2: Extended Kalman filter algorithm.

Step	Operation
1	$\overline{X}_t = a(U_t, X_{t-1})$
2	$\overline{\Sigma}_t = A_t \Sigma_{t-1} A_t^T + Q_t$
3	$K_t = \overline{\Sigma}_t B_t^T (B_t \overline{\Sigma}_t B_t^T + R_t)^{-1}$
4	$X_t = \overline{X}_t + K_t(Z_t - b(\overline{X}_t))$
5	$\Sigma_t = (I - K_t B_t)\overline{\Sigma}_t$
6	Return to step 1 for next time step

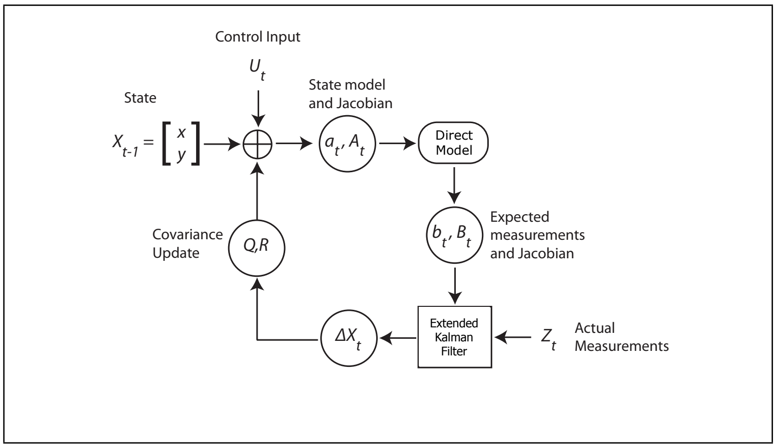

Figure 8: Parameter estimate update process using a the extended Kalman filter and a direct model.

Table 3: Adaptive extended Kalman filter algorithm.

Step	Operation
1	$\overline{X}_t = a(U_t, X_{t-1})$
2	$\overline{\Sigma}_t = A_t\Sigma_{t-1}A_t^T + Q_t$
3	$K_t = \overline{\Sigma}_t B_t^T(B_t\overline{\Sigma}_t B_t^T + R_t)^{-1}$
4	$X_t = \overline{X}_t + K_t(Z_t - b(\overline{X}_t))$
5	$\Sigma_t = (I - K_t B_t)\overline{\Sigma}_t$
6	$Q_{t+1} = \begin{cases} Q_t * M_t & \text{if } \lvert\Delta\Sigma_t\rvert > \Sigma_{tolerance} \text{ and } \Delta X_t < \Delta X_{limit} \\ Q_t/M_t & \text{if } \lvert\Delta\Sigma_t\rvert > \Sigma_{tolerance} \text{ and } \Delta X_t \geq \Delta X_{limit} \\ Q_t & \text{if } \lvert\Delta\Sigma_t\rvert \leq \Sigma_{tolerance} \end{cases}$
7	Return to Step 1 for next time step

3.3 Adaptive extended Kalman filter

Examining the extended Kalman filter algorithm (Table 2), if the measurement covariance is known with a small uncertainty, the state model covariance is unknown, and the state model covariance and measurement covariance are correlated, changes can be made during each iteration to the state model covariance to improve convergence. A value is needed from the extended Kalman filter to drive changes to the state model covariance. Two possible sources exist in the EFK algorithm: the Kalman gain (K_t) and the state covariance (Σ_t). The Kalman gain specifies the degree that the measurement update Z_t is incorporated into the new state estimate X_t while the state covariance Σ_t represents the uncertainty in the new state estimate X_t.

An adaptive extended Kalman filter was developed Myers et al. [2012a] and is presented in Table 3 and illustrated in Figure 9. Step 6 is the only change from the extended Kalman filter. The state model covariance matrix Q is modified at the end of each iteration based on the state covariance Σ and the rate of change in the estimated state ΔX_t. Three conditions are possible when modifying Q. First, if the covariance is increasing at a rate greater than a predefined tolerance value and if the estimated state is changing less than a predefined limit, Q is multiplied by an predefined adaptive gain M. This adaptive gain will have a value greater than 1, which, in this first condition, has the effect of increasing the magnitude of Q and increasing the rate of convergence. From the analysis above, an increasing state covariance Σ indicates the solution is not converged and if the change in the estimate state is below a threshold, convergence time can be reduced by increasing the magnitude of Q. Second, if the covariance is increasing at a rate greater than a predefined tolerance value and if the estimated state is changing more than a predefined limit, Q is divided by the predefined gain M. In this second condition, increasing the magnitude of Q might cause erratic convergence or a failure to reach a solution. Thus, by reducing the magnitude of Q, convergence is dampened. Third, if the covariance is increasing at a rate less than a predefined tolerance value, no change is needed to Q.

3.4 Extended Information Filter

The extended information filter is also called the information form of the Kalman filter. The key difference between the extended Kalman filter and the extended information filter is the way the Gaussian belief is represented. In the extended Kalman filter, the Gaussians are represented by their mean and covariance moments. In the extended information filter, the Gaussians are represented by their canonical parameterization where

$$\Omega = \Sigma^{-1} \qquad \phi = \Sigma^{-1}\mu \tag{5}$$

Ω is called the information matrix and ϕ is the information vector. The mean and covariance of the Gaussian can be obtained from the canonical parameterization by

$$\Sigma = \Omega^{-1} \qquad X = \Omega^{-1}\phi \tag{6}$$

The algorithm is presented in Table 4. U_t, $a(U_t, X_{t-1})$, A_t, $b(\overline{X}_t)$, B_t, Q_t, and R_t are identical to those in the extended Kalman filter. The prediction is implemented in steps 1 through 3 while the correction is implemented in steps 4 through 6.

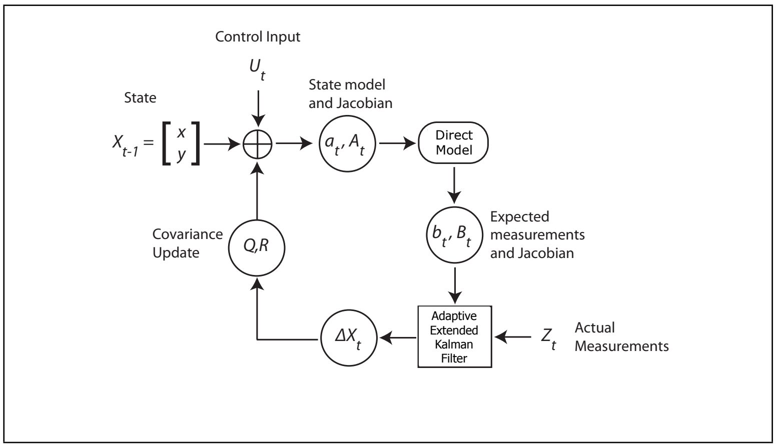

Figure 9: Parameter estimate update process for the adaptive extended Kalman filter and a direct model.

Table 4: Extended information filter algorithm.

Step	Operation
1	$X_{t-1} = \Omega_{t-1}^{-1}\phi_{t-1}$
2	$\overline{\Omega}_t = (A\Omega_{t-1}^{-1}A^T + Q)^{-1}$
3	$\overline{\phi}_t = \overline{\Omega}_t a(U_t, X_{t-1})$
4	$\overline{X}_t = a(U_t, X_{t-1})$
5	$\Omega_t = \overline{\Omega}_t + B^T R^{-1} B$
6	$\phi_t = \overline{\phi}_t + BR^{-1}[Z_t - b(\overline{X}_t) + B\overline{X}_t]$
7	Return to step 1 for next time step

The extended information filter is polynomial in measurement dimensionality k and state dimensionality $n : O(k^2 + n^{2.4})$. Comparison with the extended Kalman filter reveals the duality the these two filters. The measurement update is the difficult step in the extended Kalman filters because it requires a matrix inversion of a large matrix for every iteration. The extended information filter possesses an advantage of allowing R^{-1} to be computed once and reused for all iterations.

Figure 10 illustrates the parameter estimate update process for an extended information filter and a direct model. The estimated state is $X_t = [x_s, y_s]^T$ where x_s and y_s represent the estimated parameters of interest at time t.

3.5 Particle Filter

The particle filter is an alternative nonparametric implementation of the Bayes filter and is a Monte Carlo technique used for the solution of state estimation problems. The main idea is to represent the required posterior density function by a set of random samples with associated weights and to compute the estimates based on these samples and weights Vianna et al. [2010]. Figure 11 illustrates how particles are used to represent the belief. The lower right graph in Figure 11 shows samples drawn from a Gaussian random variable, x. The samples are passed through the nonlinear function $y = g(x)$ shown in the upper right graph. The resulting samples are distributed according to the random variable y which is the actual posterior density function. Figure 11 can be compared to the illustration of extended Kalman filter in Figure 7 where the posterior density function is approximated with a Gaussian. Because it is nonparametric, the particle filter can represent a much broader space of distributions than Gaussians and has the ability to model nonlinear transformations of random

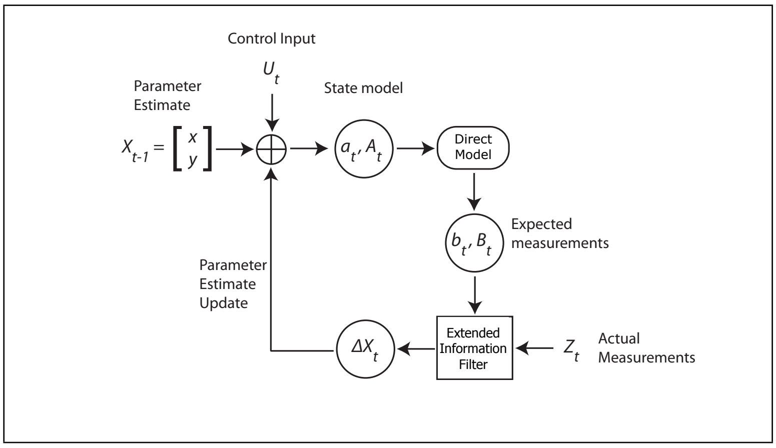

Figure 10: Parameter estimate update process using the extended information filter and a direct model.

Table 5: Particle filter algorithm.

Step	Operation
1	Generate m random possible parameters of interest (particles)
2	Obtain expected measurements for each particle i for the current time t ($Z_{i,t}$)
3	Obtain actual measurements for the current time ($Ztrue_t$)
4	Weight each particle i according to $N(Ztrue_t, I)$
5	Normalize weights for each particle i into bins from 0 to 1
6	Resample best particles using normal distribution
7	Add position noise to each particle
8	Return to Step 2 for next time step

variables Thrun et al. [2006]. The particle filter algorithm to locate the source can be found in Table 5.

Figure 12 illustrates the parameter estimate update process for a particle filter and a direct model. The estimated state is $X_t = [x_s, y_s]^T$ where x_s and y_s represent the estimated parameters of interest at time t.

3.6 Least Squares

Ordinary least squares is applied to approximate solutions of overdetermined systems, i.e. systems of equations in which there are more equations than unknowns. Ordinary least squares is often applied in statistical contexts, particularly regression analysis. Ordinary least squares may be interpreted as a method of fitting data. The best fit, between modeled data and observed data, in its least-squares sense, is an instance of the model for which the sum of squared residuals has its least value, where a residual is the difference between an observed value and the value provided by the model. The method was first described by Carl Friedrich Gauss around 1794 Bretscher [1995]. Ordinary least squares corresponds to the maximum likelihood criterion if the experimental errors have a normal distribution and can also be derived as a method of moments estimator Woodbury [2003a].

The ordinary least squares method is sometimes called the ÃGauss method of minimizationÃ Woodbury [2003a]. For a given state X, the value of T at $X = X + \Delta X$ is obtained through the truncated Taylor's series as

$$T|_{X+\Delta X} \approx T|_X + \left.\frac{\partial T}{\partial X}\right|_X \Delta X. \tag{7}$$

The ordinary least squares objective function is

$$S = (Y - T|_X - B\Delta X)^T (Y - T|_X - B\Delta X). \tag{8}$$

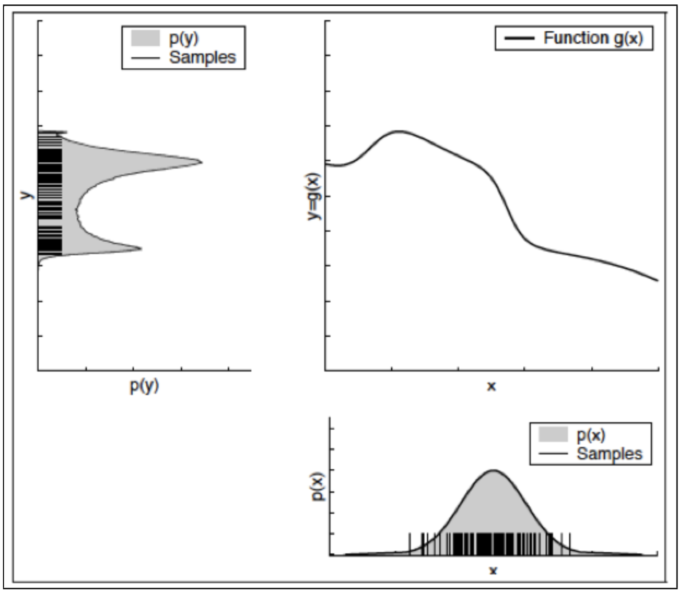

Figure 11: Illustration of how the particle filter represents the posterior density function Thrun et al. [2006].

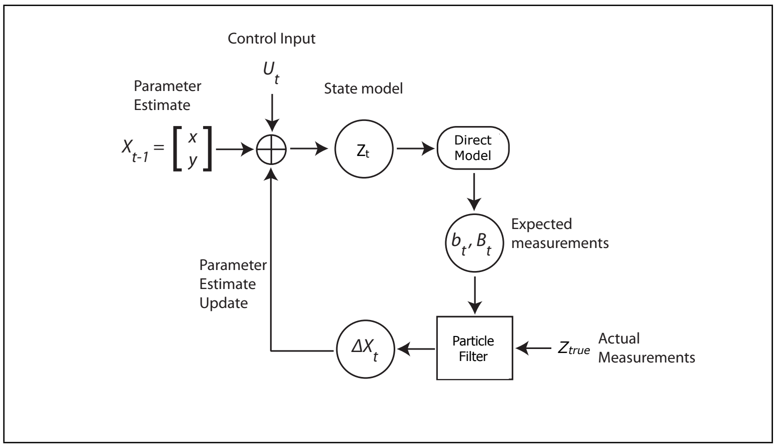

Figure 12: Parameter estimate update process using the particle filter and a direct model.

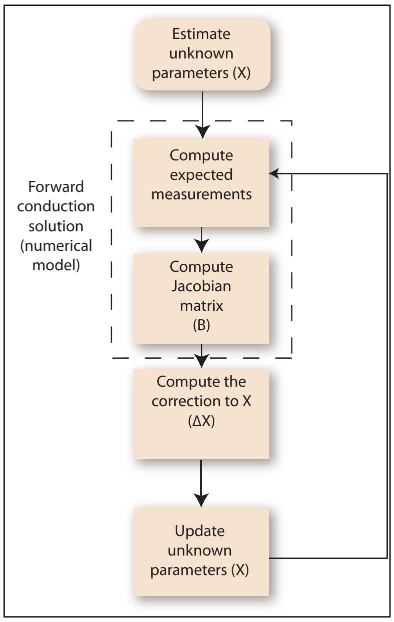

Figure 13: Ordinary least squares algorithm.

The minimizer of equation 8 is found by forcing to zero the derivative with respect to ΔX resulting in the estimator

$$\Delta X = (B^T B)^{-1} B^T (Y - T|_X). \tag{9}$$

The sensitivity matrix B can be normalized to produce a better conditioned matrix for the inversion in equation 9. As illustrated in Figure 13, X is updated using ΔX and a new ΔX is computed. Once each component in ΔX is small, the solution is converged yielding our estimate for the unknown parameters.

Figure 13 illustrates the parameter estimate update process for a least squares and a direct model. The estimated state is $X_t = [x_s, y_s]^T$ where x_s and y_s represent the estimated parameters of interest at time t.

4 Measurement Models

Different measurement methods and sensors are available when estimating a quantity of interest such as movement, speed, acceleration, vibration, temperature, heat flux, ultrasonic signal propagation time, and x-ray profile. This section details heating source experiments to demonstrate and develop measurement models for use with inverse methods in detection, localization, and parameter estimation.

Consider a $61cm$ x $30.5cm$ x $0.635cm$ stainless steel 316L plate (Figure 14) with constant properties (Table 6). Four K-type thermocouples are attached on one side and four on the other. With plate center being the origin and the x-axis being the length (Figure 14), thermocouples were attached at (x, y) locations of ($1cm$, $1cm$), ($2cm$, $2cm$), ($3cm$, $3cm$), and ($-1cm$, $-1cm$) on the heated side ($z = 0$) and on the non-heated side (z=0.635cm). The desire is to have thermocouple pairs in exactly the same position on either side of the plate allowing measurement of the temperature difference between the two sides. The thermocouples are secured to the plate with thermal grease and Kapton tape to ensure good thermal contact. Flat black paint is applied to a $1.5cm$ diameter area at the plate center to maximize energy absorption from the heater. The plate is oriented vertically with the positive y-axis pointing up. A Research, Inc. SpotIR® 4150 heater with focusing cone is positioned approximately $2mm$ from the plate surface such that its beam strikes the plate center. Experiments are conducted with the heater running at full-power which, according to manufacturer's specifications, produces $1.7MW/m^2$ of heat flux on the plate in a circular area $0.635cm$ in diameter. Consequently, approximately $54Watts$ of energy are being absorbed by the plate when the heater is on.

During the experiment, the heater is turned on at $t = 300s$ and turned off and removed at $t = 600s$. Data acquisition equipment is used to record thermocouple temperature readings every second during the experiment.

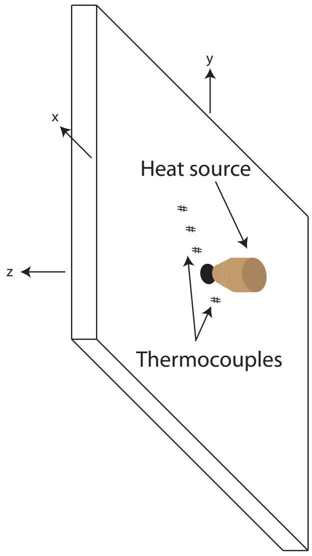

Figure 14: Illustration of flat plate with heat source and sensors (not drawn to scale).

Table 6: Material properties for the stainless steel 316L test sample used in the conduction experiments.

Property	Value
density (ρ)	$8,000 kg/m^3$
thermal conductivity (k)	$14.6 W/m\,K$
specific heat (c_p)	$500 J/kg\,K$
sound speed (v_0)	$5,100 m/s$ @ $293\,K$
ultrasonic TOF temperature factor (ξ)	$110{-}61/\,K$
sample length	61cm
sample width	30.5cm
sample height	0.635cm

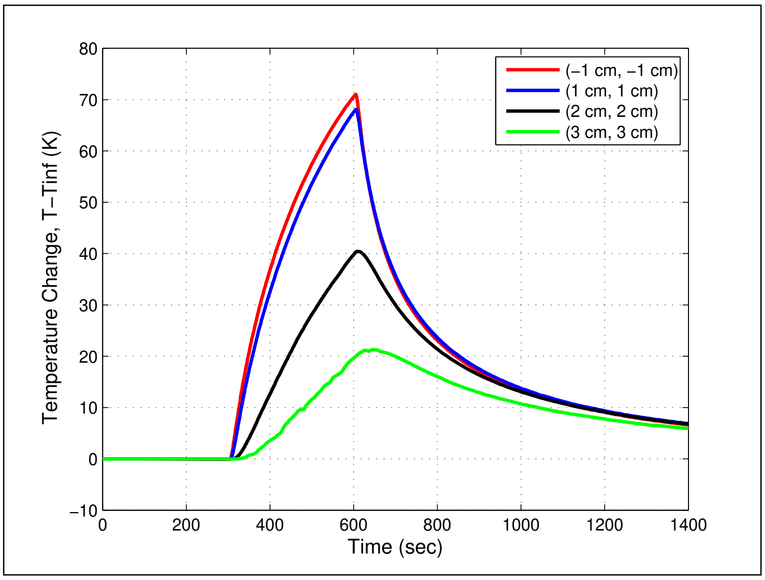

Figure 15: Temperature response on non-heated side of the plate at four sensor locations.

A MIKRON Thermo Scan TS7302 infrared camera is used to collect thermal images of the plate and heater. Coupled with a laptop computer, this system records thermal images every five seconds during the experiment. Benefits gained from the thermal images include visualization of the temperature distribution throughout the experiment and the need to model secondary convection and radiation heating in addition to modeling the primary high heat flux coming from the heater's beam. Figure 15 illustrates the thermocouple temperature data recorded during the experiment. Analysis of the data indicates that a spatial temperature gradient of $6°C/mm$ exists during heating in the area of the thermocouple sets closest to the source [$(1cm,\ 1cm)$ and $(-1cm,\ -1cm)$]. Positioning the heating source and the sensors within this degree of precision proved difficult. Therefore, sensor and heating source placement error is the most likely cause of the discrepancies between the two thermocouple sets closest to the source.

The forward conduction solution leverages COMSOL Multiphysics® by the COMSOL Group and MATLAB® by The Mathworks, Inc. The COMSOL® model uses a finite element mesh with smaller elements near the heat source and larger elements near the plate edges to conserve computing resources.

For the flat plate detailed above, the governing equation for the subdomain (conduction in the plate) is

$$\rho C_p \frac{\partial T}{\partial t} - \nabla \cdot (k \nabla T) = Q \tag{10}$$

where ∇ is the Laplacian and Q is an internal heat source (0 in this case). For the flat plate, k is assumed constant. Thus, the subdomain governing equation is

$$\nabla^2 T = \frac{\rho C_p}{k} \frac{\partial T}{\partial t} \tag{11}$$

or

$$\frac{\partial^2 T}{\partial x^2} + \frac{\partial^2 T}{\partial y^2} + \frac{\partial^2 T}{\partial z^2} = \frac{\rho C_p}{k} \frac{\partial T}{\partial t} \tag{12}$$

The boundary condition is

$$n \cdot (k \nabla T) = q_0 + h(T_{inf} - T) \tag{13}$$

where n is the surface normal vector, q_0 is the inward heat flux. Radiation effects are assumed negligible for the plate.

The first meshing method analyzed in this section is the 3D free mesh using tetrahedral elements. A $0.635cm$ diameter cylindrical subdomain in the plate's center is used to create a boundary for applying the heating source. This technique also creates small elements near the heating source and large elements far

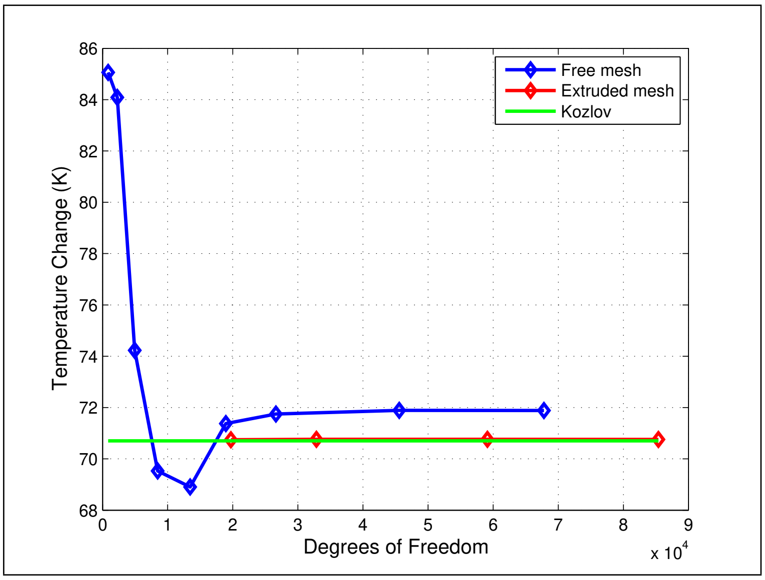

Figure 16: Grid independence results for the heated side at 1.4cm from the source and $t = 400s$.

away from the source where temperature gradients are small thereby conserving computing resources. Mesh refinement is accomplished using all of the predefined free mesh sizes available in the direct model starting with the coarsest mesh and proceeding to the finest mesh. Grid convergence is achieved with 13,256 elements and 26,628 degrees of freedom, however the solution does not agree with an analytical solution of heating through a circular domain without convection Kozlov et al. [1989] as illustrated in Figure 16. Element sizes from the converged 3D free mesh were used to create an extruded mesh which does agree the analytic solution (Figure 16). The extruded mesh is generated by first creating 2D triangle elements in the plate's $x - y$ plane and then extruding the 2D mesh in the z-direction to create prism elements. Two subdomains consisting of a $0.635cm$ diameter circle with a maximum element size of $13m$ and a $6cm$ diameter circle with a maximum element size of $5{-}3m$ were used. The 2D mesh is created with the predefined normal free mesh setting in the direct model. The mesh extrusion process incorporates an option to create multiple mesh layers, therefore grid independence is contingent upon the number of layers through the thickness of the plate. The worst case is where the highest temperature gradients through the plate's thickness exist which is located at plate center. Figure 17 illustrates the computed temperature profile through the plate at plate center with one, two, four, and six mesh layers. The grid convergence study led to the selection of three mesh layers through the plate's thickness dimension, 9,780 total elements, and 45,983 degrees of freedom. Agreement between the final the direct model solution and the closed-form solution Kozlov et al. [1989] is acceptable with mean absolute error less than $0.5K$.

Even with manufacturer specifications, the heat transfer between the radiative heater and the plate is not known with much certainty. Further complicating matters, the heater's proximity to the plate implies an unknown amount of secondary radiation and convection heating on the plate. The focusing cone reaches temperatures in excess of $200°C$ and the lamp is cooled with forced air that exits the heater through the focusing cone pointed at the plate. Based on the focusing cone temperature and a focusing cone area of $20cm^2$, approximately $2.5W$ of radiation and convection energy are absorbed by the plate outside of area illuminated by the lamp. If we assume the area affected by this secondary heating is a circle with a radius of $9cm$, we can approximate the secondary heating with a Gaussian profile of $q''_g = 100W/m^2$ and $\sigma_g^2 = 0.0009m^2$. Figure 18 illustrates the boundary conditions used in modeling the plate. For this initial analysis, the main heat flux and convection coefficient are estimated. The convection coefficient being estimated is the average value over the duration of the experiment. While areas of the heated side of the plate may have a different convection coefficient value during heating, once the heater is removed, the average convection coefficient is identical on both sides of the plate. Thus, the heat transfer coefficient h is assumed constant and identical on both sides of the plate. Estimating h using free convection correlations Incropera and DeWitt [2002] produces an expected range of $2W/m^2K \leq h \leq 5W/m^2K$. Since the plate edges do not contribute significantly to the thermal load,

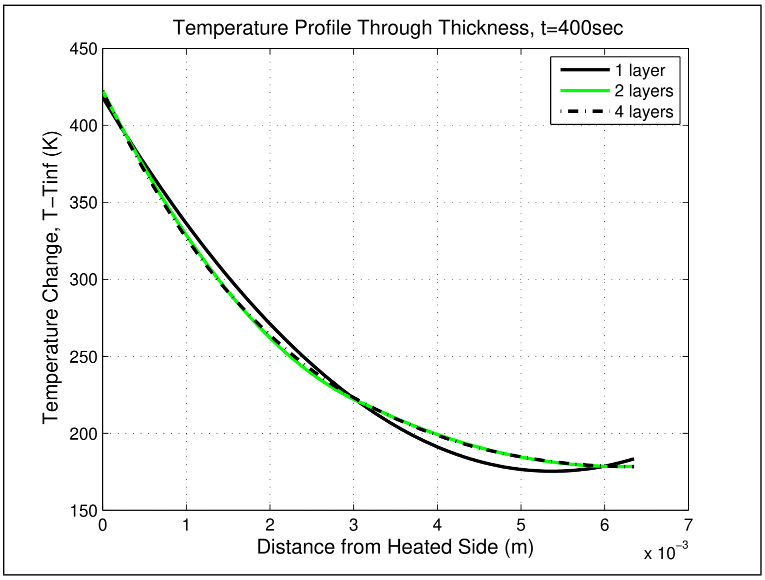

Figure 17: Number of mesh layers for best accuracy.

$h = 3W/m^2K$ is assumed on all four plate edges.

Three inverse methods are compared to quantify the heat flux (q'') and convection coefficient (h) on the plate: least squares, extended Kalman filter, and extended information filter. For the inversion, the entire experiment is treated as one event and temperature measurements are combined together. The experiment covers 1,400 seconds and data are recorded at one second intervals. Not all of the data is needed for the inverse and longer time steps can be used during periods of little thermal activity. Accordingly, one measurement at $t = 0s$, one measurement per second from $t = 290$ to $800s$ (the heater is on from $t = 300$ to $600s$), and one measurement per five seconds from $t = 805$ to $1,400s$ is used. The 5,056 temperature measurements therefore are effectively 5,056 separate sensors. All three methods start with an initial guess of the state $x_0 = [q''\ h]^{\mathrm{T}} = [1.7MW/m^2\ 5.0W/m^2K]^{\mathrm{T}}$ and are processed recursively to convergence.

For least squares, the estimated temperatures T for each sensor location and for each time t, a $5,056 \times 1$ matrix, depend on a vector of two unknowns in the state X and the value of T at $X = X + \Delta X$ is obtained through the truncated Taylor's series as Woodbury [2003b]

$$T|_{X+\Delta X} \approx T|_X + \left.\frac{\partial T}{\partial X}\right|_X \Delta X. \tag{14}$$

The gradient coefficient in equation 14 is the $5,056 \times 2$ sensitivity matrix

$$B = \frac{\partial T}{\partial X} = \begin{bmatrix} \frac{\partial T_1}{\partial q''}q'' & \frac{\partial T_1}{\partial h}h \\ \frac{\partial T_2}{\partial q''}q'' & \frac{\partial T_2}{\partial h}h \\ \vdots & \vdots \\ \frac{\partial T_{5,056}}{\partial q''}q'' & \frac{\partial T_{5,056}}{\partial h}h \end{bmatrix} \tag{15}$$

which has been normalized to have units of temperature producing a better conditioned matrix for the inversion in the least squares estimator $\Delta X = (B^TB)^{-1}B^T(Y - T|_X)$ Woodbury [2003b].

The direct numerical model produces values of T based on current estimates for the state X. The sensitivity matrix B is obtained using finite differences (a $5,056 \times 2$ matrix) by independently varying the state parameters 0.1%. We designate our experimentally obtained temperature measurements as Y, a $5,056 \times 1$ matrix. Our goal is to improve the estimate for the state X based on the observations Y.

The algorithm for the extended Kalman filter is listed in Table 2 where $\overline{X}_t$ is the predicted state, $a(U_t, X_{t-1})$ is the state model based on the input U_t and the previous state X_{t-1}, A is the state model Jacobian, $\overline{\Sigma}$ is the uncertainty estimate, Q_t is the state model covariance, K_t is the Kalman gain, B_t is the measurement Jacobian,

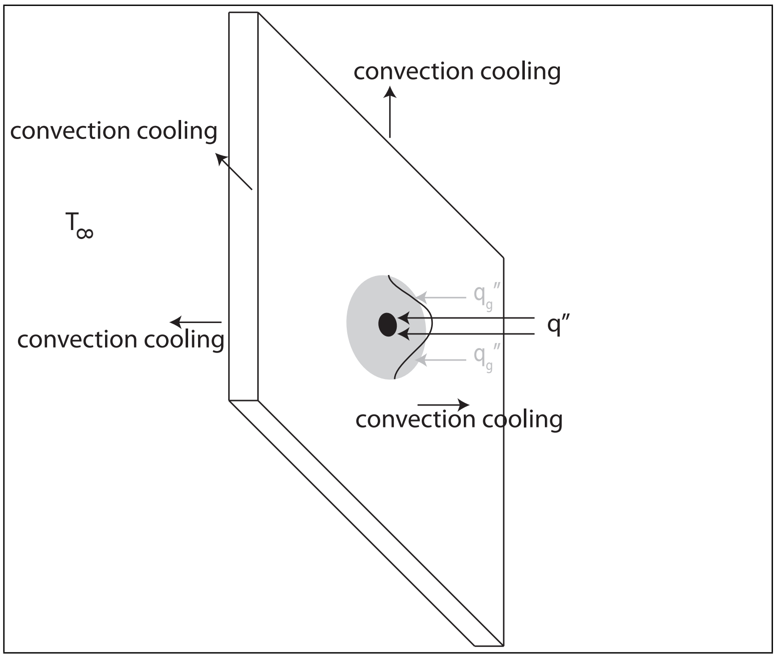

Figure 18: Illustration of boundary conditions on the flat plate.

R_t is the measurement covariance, $b(\overline{X}_t)$ is the measurement transition function and represents the predicted measurements from the forward conduction solution based on the predicted state, and Z_t represents the actual measurements. The filter represents the belief at time t by the state X_t and the covariance Σ_t. For the flat plate considered here, there is no input to the state thus the state model is $a = I_2$ and the state model Jacobian is $A = I_2$, where I_2 is a 2×2 identity matrix. The measurement transition function b is a $5,056 \times 1$ matrix of the predicted temperatures from the forward conduction solution, and the measurement Jacobian B is obtained using finite differences (a $5,056 \times 2$ matrix) by independently varying the state parameters 0.1%. The state model covariance matrix Q is a 2×2 diagonal matrix using $\sigma_q^2 = 0.1MW^2/m^4$ and $\sigma_h^2 = 0.1W^2/m^4K^2$. These values were chosen through a parameter sweep to achieve smooth convergence behavior since small values for the state model covariance matrix cause the Gaussian filters to diverge while arbitrarily large values for the state model covariance matrix render the Gaussian filters essentially identical to the least squares method. The thermocouples have a measurement accuracy of $\pm 1.5°C$, which translates to a measurement variance of $\sigma_T^2 = 0.25°C^2$. This value is used for the diagonal elements of the measurement covariance matrix R, a $5,056 \times 5,056$ matrix. The filter is initialized with the initial state x_0 (stated above) and covariance $\Sigma_0 = 0$. For the extended information filter (Table 4), a, A, b, B, R, and Q are identical to those in the extended Kalman filter. The extended information filter possesses an advantage of allowing the inverse of the measurement covariance matrix Q^{-1} to be computed once and reused for all iterations. Because the initial state covariance matrix Σ_0 is inverted in the extended information filter, the filter is initialized with $\Sigma_0 = R$ instead of the zero matrix used to initialize the extended Kalman filter.

Figures 19 and 20 illustrate the convergence behavior for all three methods. The extended Kalman filter and extended information filter converge identically and are presented together. The Gaussian filters converge a bit slower than the least squares method, however the convergence is smoother. Once convergence is achieved, statistical moments are computed from the last three iterations (Figure 21). Results are similar for all three methods. The least squares method uses the least amount of wall time and memory of the three methods. Wall time for each iteration, independent of recomputing the direct model for the updated parameters, is approximately two orders of magnitude longer for extended information filter and four orders of magnitude longer for extended Kalman filter than the wall time for least squares. Memory usage is approximately 1.5 times more for extended information filter and 2 times more for extended Kalman filter than the memory required by least squares. When considering convergence behavior and computational cost, least squares outperforms the other methods for this type of parameter estimation.

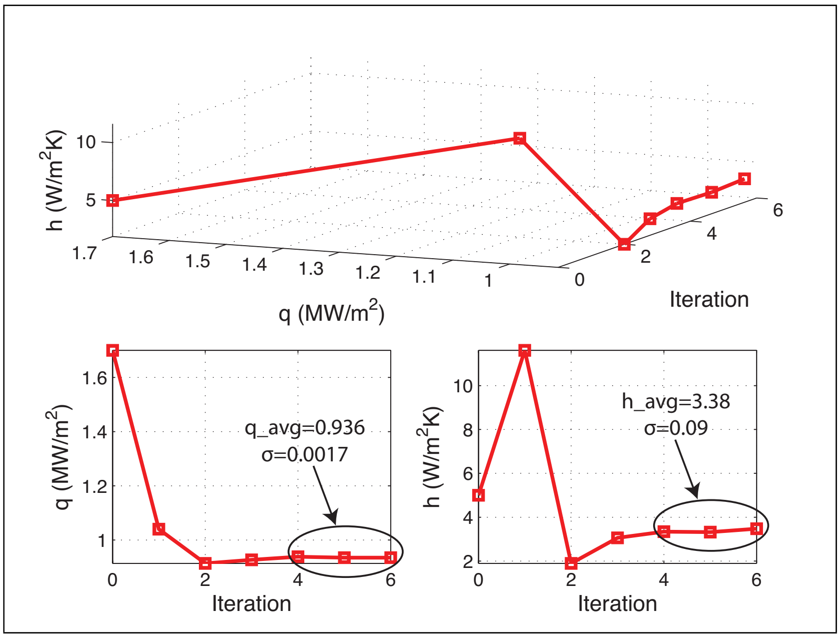

Figure 19: Least squares convergence.

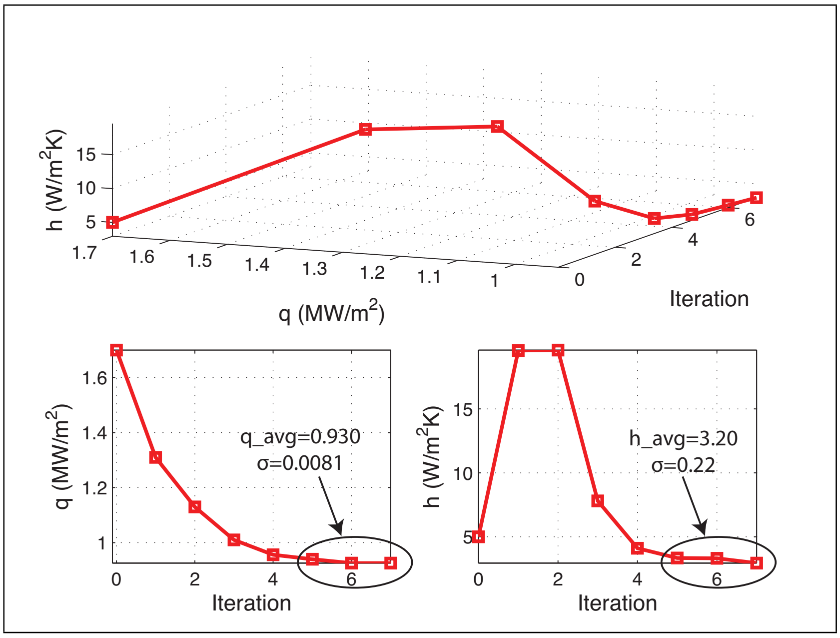

Figure 20: Extended Kalman filter and extended information filter convergence. The filters produce identical results and are presented together.

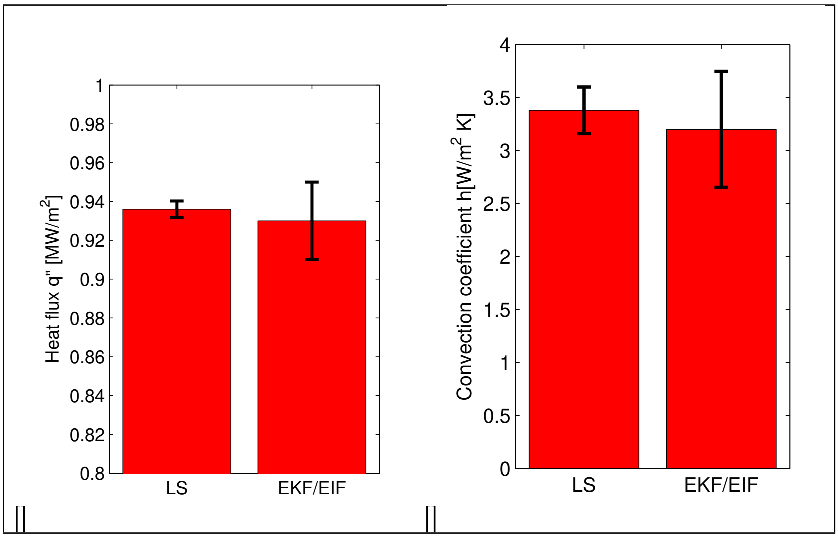

Figure 21: Statistical moments from parameter identification for (a) heat flux q'' and (b) convection coefficient h comparing least squares, extended Kalman filter, and extended information filter.

Figure 22 compares the temperature response measured during the experiment with the temperature response of the model using the results of the estimation (i.e., $q'' = 0.930 MW/m^2$ and $h = 3.20 W/m^2\,K$). The residuals Beck and Woodbury [1998], Dowding and Blackwell [2001] are illustrated in Figure 23. Agreement between the model and the experiment is acceptable, however improvement could be achieved through modifications to the heating profile (e.g., secondary heating). Agreement with the experiment is better when simultaneously estimating q'' and h than when estimating q'' with h arbitrarily fixed.

A check of the boundary effect errors is conducted to ensure the plate is sized sufficiently large (Figure 24). Of particular interest is in the region of ($\pm 4cm$,$\pm 4cm$) where the errors remain well below 0.5% for the entire experiment. Even at ($\pm 10cm$,$\pm 10cm$), the errors are below 1% for much of the experiment and stay below 3% for the entire experiment.

4.1 Measurement model selection

One important question in this analysis is determining if an ultrasound-based solution can outperform a thermocouple solution. This section seeks to answer this question by examining six measurement models, two incorporating thermocouples and four incorporating ultrasonic transducers. The following six measurement models have been identified for analysis and will be detailed in the following sections:

1. Temperature measurement model
2. Radius from temperature measurement model
3. Ultrasonic pulse-echo time of flight measurement model
4. Radius from ultrasonic pulse-echo time of flight measurement model
5. Ultrasonic pulse one-way time of flight measurement model
6. Ellipse from ultrasonic one-way pulse time of flight measurement model

These measurement models represent different ways to collect measurements (sensors) and different ways to process the data. Comparison of the six measurement models is performed using the extended Kalman filter (algorithm in Table 2) to locate the source (x_q, y_q). For all six measurement models, the estimated state is $X_t = [x_s, y_s]^T$ where x_s and y_s represent the estimated location of the source at time t. There is no input to the

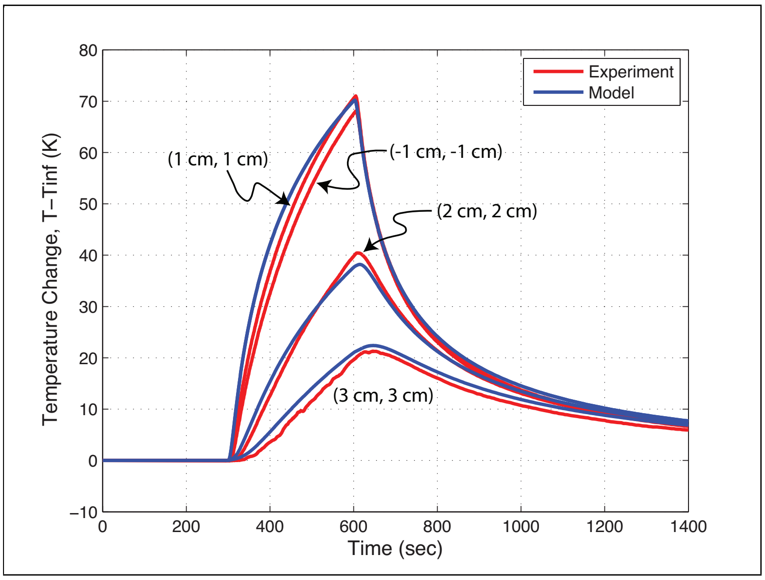

Figure 22: Comparison of the temperature response on non-heated side of the plate at four sensor locations.

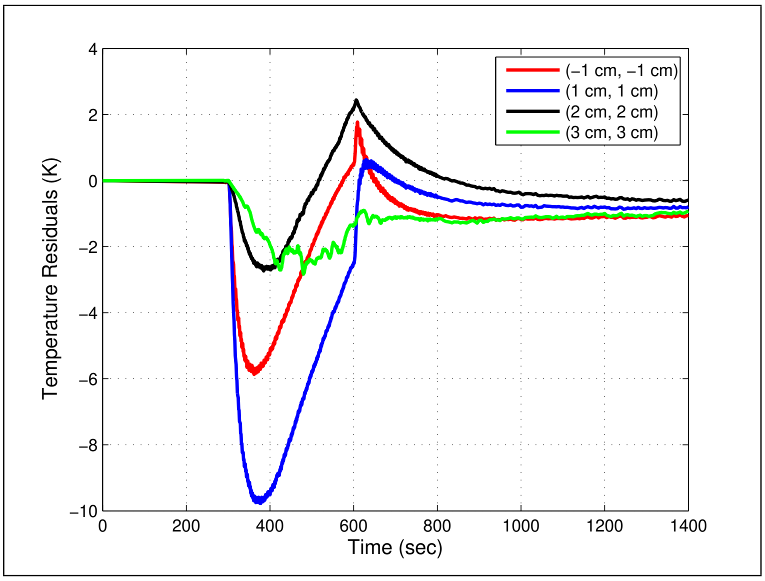

Figure 23: Residuals of the model when compared to the experiment measurements on the non-heated side.

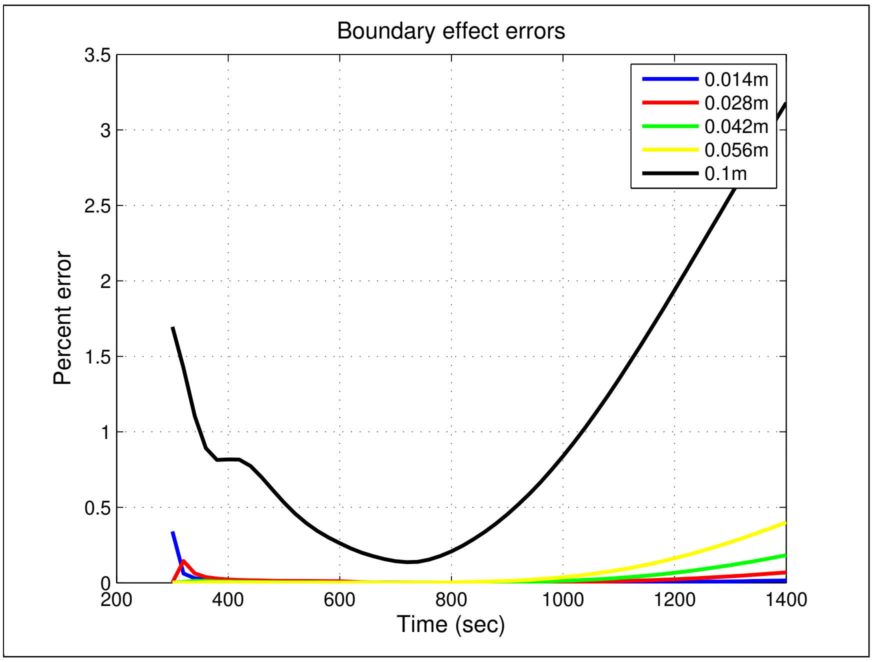

Figure 24: Illustration of when and where the plate edges introduce errors in the temperature distribution.

state thus the state model is $a = I_2$ and the state model Jacobian is $A = I_2$. Sensitivity of the state variance is compared for values from $\sigma^2 = 0.01m^2$ to $0.000001m^2$ with the lower values providing a damping effect. A state variance of $\sigma^2 = 0.0001m^2$ provides smooth, fast convergence without producing erratic convergence behavior exhibited by the higher state variance values and will be used for all measurement model comparisons in this section. Thus, the state model covariance matrix is $Q_t = 0.0001m^2 * I_2$, where I_2 is a 2×2 identity matrix.

Locating and characterizing a heating source depends upon many factors such as heating source movements in time, heating source magnitude changes in time, and other transient behaviors. Fairly restrictive assumptions can be imposed that simplify the problem. Analysis and algorithm development can proceed using these restrictive assumptions and then assumptions can be relaxed in stages to achieve the end result of source localization and characterization. The assumptions for this section are:

1. Source in fixed position (location unknown)
2. Source applied at time $t = 300s$ and removed at $t = 600s$
3. $q'' = 0.930MW/m^2$ over $0.00635m$ diameter circular area while source applied (value obtained in parameter estimation above)
4. Secondary heating is characterized by a Gaussian with magnitude $q''_g = 100W/m^2$ and variance $\sigma_g^2 = 0.0009m^2$ while source applied
5. Convection coefficient $h = 3.20W/m^2K$ on both sides of the plate (value obtained in parameter estimation above)
6. Convection coefficient $h = 3W/m^2K$ on the plate edges
7. Thermal conductivity $k = 15W/mK$
8. Specific heat $C_p = 500J/kgK$ and density $\rho = 8,000kg/m^3$
9. Positions of sensors are $(\pm 4cm, \pm 4cm)$ on the non-heated side

4.2 Temperature measurement model

In this direct model, temperatures are measured using four thermocouples on the non-heated side of the plate. Expected temperatures and the partial derivatives are obtained directly from the direct model to form the measurement transition function $b(\overline{X}_t)$ and the Jacobian B_t.

$$b(\overline{X}_t) = \begin{bmatrix} \bar{\theta}_1 \\ \bar{\theta}_2 \\ \bar{\theta}_3 \\ \bar{\theta}_4 \end{bmatrix} \tag{16}$$

$$B_t = \begin{bmatrix} -\frac{\partial \bar{\theta}_1}{\partial x_1} & -\frac{\partial \bar{\theta}_1}{\partial y_1} \\ -\frac{\partial \bar{\theta}_2}{\partial x_2} & -\frac{\partial \bar{\theta}_2}{\partial y_2} \\ -\frac{\partial \bar{\theta}_3}{\partial x_3} & -\frac{\partial \bar{\theta}_3}{\partial y_3} \\ -\frac{\partial \bar{\theta}_4}{\partial x_4} & -\frac{\partial \bar{\theta}_4}{\partial y_4} \end{bmatrix} \tag{17}$$

where t is time in seconds with a time step of $1s$, $\bar{\theta}$ is the expected change in temperature relative to a reference, obtained from the direct model, if the heating source is located at (x_s, y_s), and (x_i, y_i) with $i = 1, 2, 3, 4$ indicating the locations of the four thermocouples. The Jacobian B_t is constructed using the derivatives with respect to sensor position for convenience since this information can be obtained with one direct model simulation. The derivatives are obtained directly from the direct model. Based on the flat plate experiment above, sensor noise is assumed be $\pm 0.045K$ and is normally distributed ($\sigma^2 = (0.045/3)^2 = 2.225{-}4K^2$). The measurement covariance matrix is $R = 2.225{-}4K^2 * I_4$.

4.3 Radius from temperature measurement model

This indirect model is similar to the previous model in that temperatures are measured using thermocouples, but in this model, the direct model is used as a lookup table to convert measured temperatures to a radius from each sensor to the source. Knowledge of the heating start time, one of the assumptions in this section, enables a simple direct model lookup of expected temperatures for a range of radius values from the heating source. Linear interpolation is used with this lookup table to obtain an expected radius for each temperature measurement.

$$r_i = \sqrt{(x_i - x_s)^2 + (y_i - y_s)^2} \tag{18}$$

where (x_i, y_i) is the location of sensor i for $i = 1, 2, 3, 4$ and (x_s, y_s) the heating source location. The Jacobian is based solely on geometry, which may reduce errors.

$$\begin{aligned} \frac{\partial r_i}{\partial x_s} =& \frac{1}{2}\left((x_i - x_s)^2 + (y_i - y_s)^2\right)^{-\frac{1}{2}} \\ & \left(\frac{\partial}{\partial x_s}(x_i^2 - 2x_i x_s + x_s^2)\right) \end{aligned} \tag{19}$$

$$\frac{\partial r_i}{\partial x_s} = \frac{x_s - x_i}{r_i}, \frac{\partial r_i}{\partial y_s} = \frac{y_s - y_i}{r_i} \tag{20}$$

The measurement transition function $b(\overline{X}_t)$ and the Jacobian B_t are then

$$b(\overline{X}_t) = \begin{bmatrix} \sqrt{(x_1 - x_s)^2 + (y_1 - y_s)^2} \\ \sqrt{(x_2 - x_s)^2 + (y_2 - y_s)^2} \\ \sqrt{(x_3 - x_s)^2 + (y_3 - y_s)^2} \\ \sqrt{(x_4 - x_s)^2 + (y_4 - y_s)^2} \end{bmatrix} \tag{21}$$

$$B_t = \begin{bmatrix} \frac{x_s - x_1}{r_1} & \frac{y_s - y_1}{r_1} \\ \frac{x_s - x_2}{r_2} & \frac{y_s - y_2}{r_2} \\ \frac{x_s - x_3}{r_3} & \frac{y_s - y_3}{r_3} \\ \frac{x_s - x_4}{r_4} & \frac{y_s - y_4}{r_4} \end{bmatrix} \tag{22}$$

where t is time in seconds with a time step of $1s$, $\overline{r}_i$ with $i = 1, 2, 3, 4$ is the radius from the sensor to the source, obtained from the direct model, if the source is located at (x_s, y_s), and (x_i, y_i) with $i = 1, 2, 3, 4$ indicating the locations of the four thermocouples. Based on the flat plate experiment above, sensor noise is assumed be $\pm 0.045K$ and is normally distributed ($\sigma^2 = (0.045/3)^2 = 0.000225K^2$). Since measured temperature is being related to radius, sensor noise must be converted into radius noise. The complication in this conversion arises from the fact that radius is a non-linear function of temperature and time. Based on insights gained from the forward conduction model and analysis of the temperature response in the plate, a value of $0.015m/K$ is used resulting in a radius noise of $\pm 0.000675m$ with normal distribution ($\sigma^2 = 5.06{-}8m^2$). The measurement covariance matrix, therefore, is $R = 5.06{-}8m^2 * I_4$.

4.4 Ultrasonic pulse-echo time of flight measurement model

This direct model uses ultrasonic pulses to measure the average temperature through the material thickness at each sensor location. In the pulse-echo method, the ultrasonic pulse travels through the material thickness, reflects off the boundary, and returns to the transducer. The time of flight is Myers et al. [2008, in review, 2010]

$$G_{ii} = \frac{2L}{v_o} \left(1 + \xi \theta_{avg} |_0^L \right) \tag{23}$$

where L represents the material thickness, v_0 is the speed of sound in the material at a reference temperature, ξ is the ultrasonic time of flight factor which is material dependent, and θ is the change in temperature from the reference temperature. The ultrasonic pulse time of flight measurement model consists of obtaining expected temperatures from the direct model, computing the average temperature between the transducer and the boundary, and then computing an expected time of flight using equation 23 to form the measurement transition function $b(\overline{X}_t)$ (equation 24). The Jacobian partial derivatives are obtained using time of flight difference when moving the source in the x and y directions independently (equation 25).

$$b(\overline{X}_t) = \begin{bmatrix} \overline{G}_1 \\ \overline{G}_2 \\ \overline{G}_3 \\ \overline{G}_4 \end{bmatrix} \tag{24}$$

$$B_t = \begin{bmatrix} -\frac{\partial \overline{G}_1}{\partial x_1} & -\frac{\partial \overline{G}_1}{\partial y_1} \\ -\frac{\partial \overline{G}_2}{\partial x_2} & -\frac{\partial \overline{G}_2}{\partial y_2} \\ -\frac{\partial \overline{G}_3}{\partial x_3} & -\frac{\partial \overline{G}_3}{\partial y_3} \\ -\frac{\partial \overline{G}_4}{\partial x_4} & -\frac{\partial \overline{G}_4}{\partial y_4} \end{bmatrix} \tag{25}$$

where t is time in seconds with a time step of 1 second, $\overline{G}_i$ with $i = 1, 2, 3, 4$ is the expected ultrasonic pulse time of flight, obtained from the direct model, with the heating source at location (x_s, y_s), and (x_i, y_i) with $i = 1, 2, 3, 4$ indicating the locations of the four transducers. The Jacobian B_t is constructed using the derivatives with respect to sensor position for convenience since this information can be obtained with one direct model

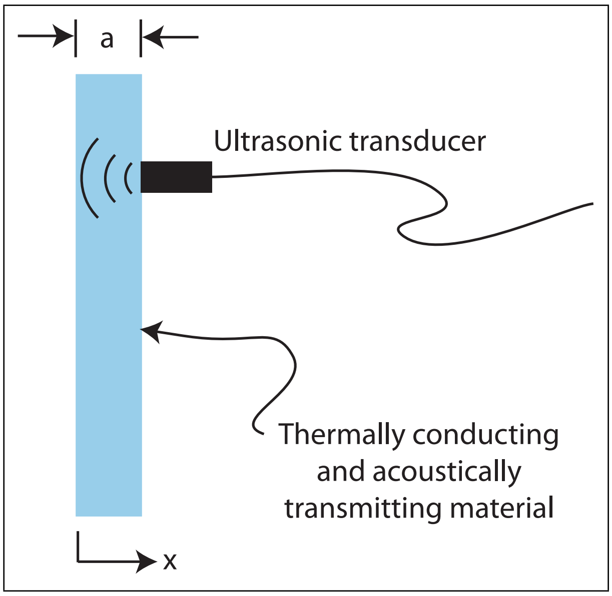

Figure 25: Ultrasonic pulse-echo technique.

simulation. The derivatives are obtained from the direct model using finite differences by independently varying the x and y positions of all sensors by $0.0001m$. Based on the flat plate experiment above, sensor noise is assumed be $\pm 2.3{-}10s$ and is normally distributed ($\sigma^2 = 5.88{-}21sec^2$). The measurement covariance matrix, therefore, is $R = 5.88{-}21sec^2 * I_4$.

4.5 Radius from ultrasonic pulse-echo time of flight measurement model

In this indirect model, ultrasonic pulse-echo time of flight is measured using four transducers on the non-heated side of the plate. Similar to radius from temperature method, this method converts the measured time of flight to a radius using the direct model as a lookup table. Knowledge of the heating start time, one of the assumptions in this section, enables a simple direct model lookup of expected temperatures for a range of radius values from the heating source. Temperatures in the plate are related to time of flight through equation 23. Linear interpolation is used with this lookup table to obtain an expected radius for each time of flight measurement. Equations 18 to 20 develop the geometry behind the measurement transition function $b(\overline{X}_t)$ and the Jacobian B_t which are

$$b(\overline{X}_t) = \begin{bmatrix} \sqrt{(x_1 - x_s)^2 + (y_1 - y_s)^2} \\ \sqrt{(x_2 - x_s)^2 + (y_2 - y_s)^2} \\ \sqrt{(x_3 - x_s)^2 + (y_3 - y_s)^2} \\ \sqrt{(x_4 - x_s)^2 + (y_4 - y_s)^2} \end{bmatrix} \tag{26}$$

$$B_t = \begin{bmatrix} \frac{x_s - x_1}{r_1} & \frac{y_s - y_1}{r_1} \\ \frac{x_s - x_2}{r_2} & \frac{y_s - y_2}{r_2} \\ \frac{x_s - x_3}{r_3} & \frac{y_s - y_3}{r_3} \\ \frac{x_s - x_4}{r_4} & \frac{y_s - y_4}{r_4} \end{bmatrix} \tag{27}$$

where t is time in seconds with a time step of 1 second, $\overline{r}_i$ with $i = 1, 2, 3, 4$ is the radius from the sensor to the source, obtained from the direct model, if the source is located at (x_s, y_s), and (x_i, y_i) with $i = 1, 2, 3, 4$ indicating the locations of the four thermocouples. Based on the flat plate experiment above, sensor noise is assumed be $\pm 2.3{-}10s$ and is normally distributed ($\sigma^2 = 5.88{-}21sec^2$). Sensor noise in terms of temperature

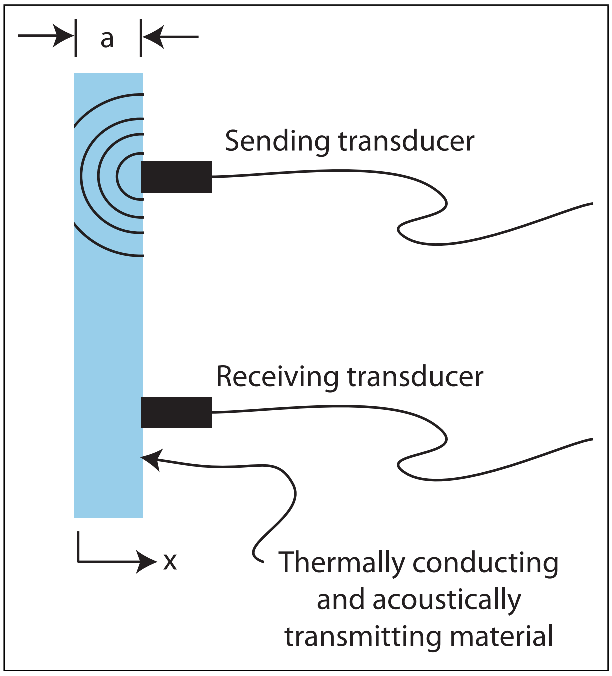

Figure 26: One-way ultrasonic pulse technique.

can be expressed as

$$\theta_{noise} = \frac{G_{noise} v_0}{2L\xi} = 0.84K \tag{28}$$

Since measured time of flight is being related to radius, sensor noise must be converted into radius noise. The complication in this conversion arises from the fact that radius is a non-linear function of time of flight and time. Based on insights gained from the forward conduction model and analysis of the temperature response in the plate, a value of $0.015m/K$ is used resulting in a radius noise of $\pm 0.0126m$ with normal distribution ($\sigma^2 = 1.76{-}5m^2$). The measurement covariance matrix, therefore, is $R_t = 1.76{-}5m^2 * I_4$.

4.6 Ultrasonic pulse one-way time of flight measurement model

Instead of sending an ultrasonic pulse through to a boundary and receiving the echo at the original transducer, one transducer can transmit the pulse and another transducer can receive the pulse. The time of flight is

$$G_{ij} = \frac{R_{ij}}{v_o} \left(1 + \xi \theta_{avg}|_i^j\right) \tag{29}$$

where R_{ij} is the distance between transducers (m). This direct measurement model consists of obtaining expected temperatures from the direct model, computing the average temperature between the transducers, and then computing an expected time of flight to form $a(U_t, X_{t-1})$ (equation 30). For the current analysis, the average temperature is based on the line on the plate surface between the two sensors. The Jacobian partial derivatives are obtained using time of flight difference when moving the source in the x and y directions

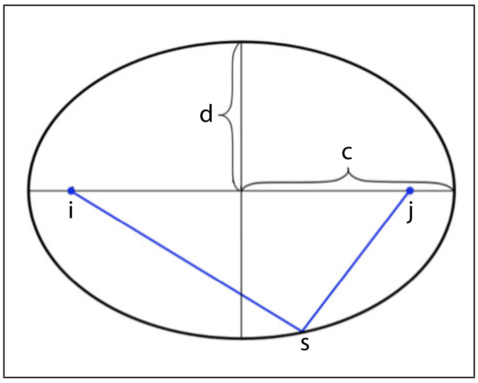

Figure 27: Ellipse properties.

independently (equation 31).

$$b(\overline{X}_t) = \begin{bmatrix} \overline{G}_1 \\ \overline{G}_2 \\ \overline{G}_3 \\ \overline{G}_4 \end{bmatrix} \tag{30}$$

$$B_t = \begin{bmatrix} -\frac{\partial \overline{G}_1}{\partial x_1} & -\frac{\partial \overline{G}_1}{\partial y_1} \\ -\frac{\partial \overline{G}_2}{\partial x_2} & -\frac{\partial \overline{G}_2}{\partial y_2} \\ -\frac{\partial \overline{G}_3}{\partial x_3} & -\frac{\partial \overline{G}_3}{\partial y_3} \\ -\frac{\partial \overline{G}_4}{\partial x_4} & -\frac{\partial \overline{G}_4}{\partial y_4} \end{bmatrix} \tag{31}$$

where t is time in seconds with a time step of $1s$, $\overline{G}_i$ with $i = 1,2,3,4$ is the ultrasonic pulse time of flight, obtained from the direct model, with the heating source located at (x_s, y_s), and (x_i, y_i) with $i = 1,2,3,4$ indicating the locations of the four transducers. The Jacobian B_t is constructed using the derivatives with respect to sensor position for convenience since this information can be obtained with one direct model simulation. The derivatives are obtained from the direct model using finite differences by independently varying the x and y positions of all sensors by $0.0001m$. Based on the flat plate experiment above, sensor noise is assumed be $\pm 1.05{-}8s$ and is normally distributed ($\sigma^2 = ((1.05{-}8)/3)^2 = 1.225{-}17sec^2$). The measurement covariance matrix, therefore, is $R = 1.225{-}17sec^2 * I_4$.

4.7 Ellipse from ultrasonic pulse one-way time of flight measurement model

In this indirect model, a particular ultrasonic pulse time of flight at a particular time after the heater is turned on means that the source could be anywhere on an assumed elliptical shape around the sensors. Figure 27 illustrates the geometry of an ellipse. The two sensors are assumed to be the focus points for the ellipse. Since the distance between sensors is known, ellipse parameters c and d can be related to each other and the ellipse can be represented with just one parameter c.

$$r_{is} + r_{js} = 2c = \sqrt{r_{ij}^2 + 4d^2} \tag{32}$$

where i and j are sensors and s is heat source.

$$c = \frac{1}{2}\sqrt{r_{ij}^2 + 4d^2} = \frac{r_{is} + r_{js}}{2} \tag{33}$$

$$r_{is} = \sqrt{(x_i - x_s)^2 + (y_i - y_s)^2} \tag{34}$$

$$r_{js} = \sqrt{(x_j - x_s)^2 + (y_j - y_s)^2} \tag{35}$$

$$\frac{\partial c_i}{\partial x_s} = \frac{1}{2}\left[\frac{x_s - x_i}{r_{is}} + \frac{x_s - x_j}{r_{js}}\right] \tag{36}$$

$$\frac{\partial c_i}{\partial y_s} = \frac{1}{2}\left[\frac{y_s - y_i}{r_{is}} + \frac{y_s - y_j}{r_{js}}\right] \tag{37}$$

The parameter c is measured indirectly by first measuring the one-way ultrasonic pulse time of flight. The forward conduction solution is used to get time of flight for a range of c values and interpolated using the spline method to obtain c for the measured time of flight. The measurement transition function $b(\overline{X}_t)$ and the Jacobian B_t are then

$$b(\overline{X}_t) = \begin{bmatrix} c_1 \\ c_2 \\ c_3 \\ c_4 \end{bmatrix} \tag{38}$$

$$B_t = \begin{bmatrix} \frac{\partial c_1}{\partial x_s} & \frac{\partial c_1}{\partial y_s} \\ \frac{\partial c_2}{\partial x_s} & \frac{\partial c_2}{\partial y_s} \\ \frac{\partial c_3}{\partial x_s} & \frac{\partial c_3}{\partial y_s} \\ \frac{\partial c_4}{\partial x_s} & \frac{\partial c_4}{\partial y_s} \end{bmatrix} \tag{39}$$

where t is time in seconds with a time step of $1s$, c_i with $i = 1, 2, 3, 4$ is the ellipse parameter if the source is located at (x_s, y_s). Based on the flat plate experiment above, sensor noise is assumed be $\pm 1.05{-}8s$ and is normally distributed ($\sigma^2 = 1.22{-}17s^2$). The sensor noise in terms of temperature can be expressed as

$$\theta_{noise} = \frac{G_{noise} v_0}{L\xi} = 6.09K \tag{40}$$

Since measured time of flight is being related to the ellipse parameter c, sensor noise must be converted into ellipse parameter noise. The complication in this conversion arises from the fact that c is a non-linear function of time of flight and time. Based on insights gained from the forward conduction model and analysis of the temperature response in the plate, a value of $0.015m/K$ is used resulting in an ellipse noise of $\pm 2.044m$ for the c parameter with normal distribution ($\sigma^2 = 4.62{-}9m^2$).

4.8 Extended Kalman filter convergence behavior

Extended Kalman filter convergence behavior for all six measurement models are compared in Figures 28 through 31. With the heating source located inside the sensor grid (Figure 28), all measurement models converge to the correct location, however both temperature measurement models exhibit rather noisy convergence. The ellipse from ultrasonic pulse one-way time of flight measurement model produces the best results with the heating source located inside the sensor grid. With the heating source located at the edge of the sensor grid (Figure 29), all measurement models once again converge to the correct location and both temperature measurement models and the radius from ultrasonic pulse-echo time of flight measurement model exhibit undesirable convergence behavior. The ellipse from ultrasonic pulse one-way time of flight measurement model produces the best results with the heating source located at the edge the sensor grid. With the heating source located outside of the sensor grid (Figure 30), none of the measurement models converge to the correct location, however the ellipse from ultrasonic pulse one-way time of flight and radius from ultrasonic pulse-echo time of flight measurement models converge to within $1cm$ of the actual location. These examples started with an initial guess of ($0cm$, $0cm$) for the heating source location. Figure 31 illustrates the convergence behavior for all six models using an

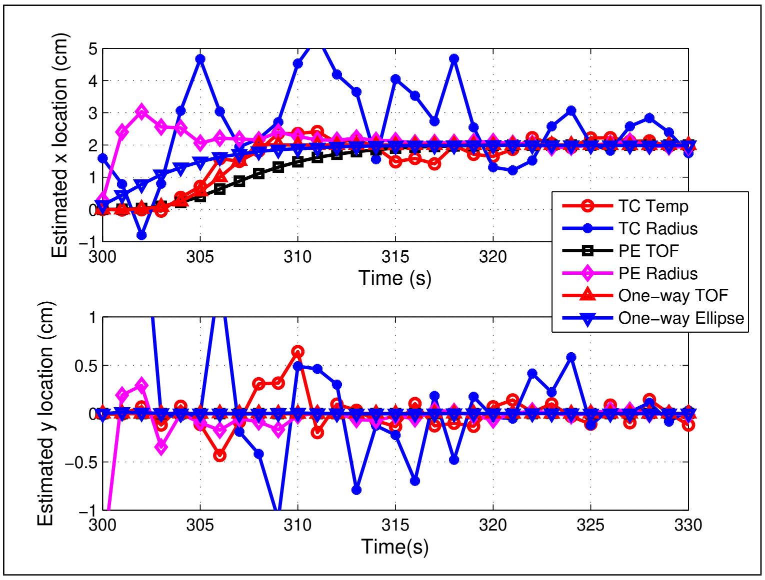

Figure 28: Extended Kalman filter convergence for all six measurement models with source at $(2cm, 0cm)$ and initial guess of $(0cm, 0cm)$.

initial guess of $(8cm, 8cm)$ for the heating source located inside the sensor grid. Interestingly, all direct models fail to converge to the correct location in this scenario. Overall, the ellipse from ultrasonic pulse one-way time of flight measurement model produces the best results when considering accuracy of converged solution, ability to converge to the correct solution given different initial guesses, and smoothness of convergence behavior.

Because we are using numerical tools to solve the governing equations, we lack a set of state equations and cannot determine the observability index in the standard fashion. We can, however, examine sensitivity to heating source location relative to sensor location as well as sensitivity to other parameters including heating source magnitude, plate thermal conductivity, and plate surface convection coefficient. Sensitivity analysis to address observability is included in Section 5.

5 Sensitivity

Sensitivity is important to understand and characterize when measuring and estimating parameters of interest. This section details sensitivity to source position, boundary conditions, and thermal conductivity from the flat plate experiments discussed in the previous section.

5.1 Sensitivity to source position

To determine the one-way pulse method's sensitivity to source location, it is necessary to examine how the average temperature between the two sensors is affected by the relative position of the heat source. Note that this discussion assumes the source is static and therefore not moving with time. Figure 32 illustrates the temperature profile on the plate's non-heated side at $t = 320s$ with the source located at $(x = 0cm, y = 0cm)$. The average temperature difference between the two sensors is $13.5K$. If the source is located at $(x = 2cm, y = 0cm)$ as in Figure 33, the average temperature difference is nearly identical at $13.2K$. We conclude, then, that even with knowledge that the source is between the sensors, its x-location cannot be determined very accurately. If the source were further to the right, say at $(x = 3cm, y = 0cm)$, the average temperature difference would be $11.8K$ indicating that sensitivity to x-location is greater close to the transducers. However, the observations do not reveal if the heat source is closer to the pulse generator or the receiver. If the source is instead offset in the y-direction at $(x = 0cm, y = 1cm)$ as in Figure 34, the average temperature difference is $5.3K$. Thus, the sensitivity to source position in the y-direction is greater than for the x-direction for this

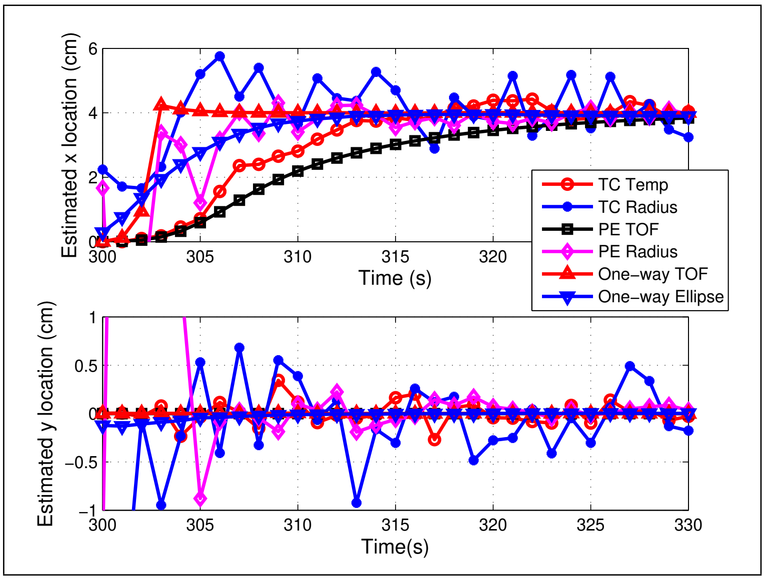

Figure 29: Extended Kalman filter convergence for all six measurement models with source at $(4cm,\ 0cm)$ and initial guess of $(0cm,\ 0cm)$.

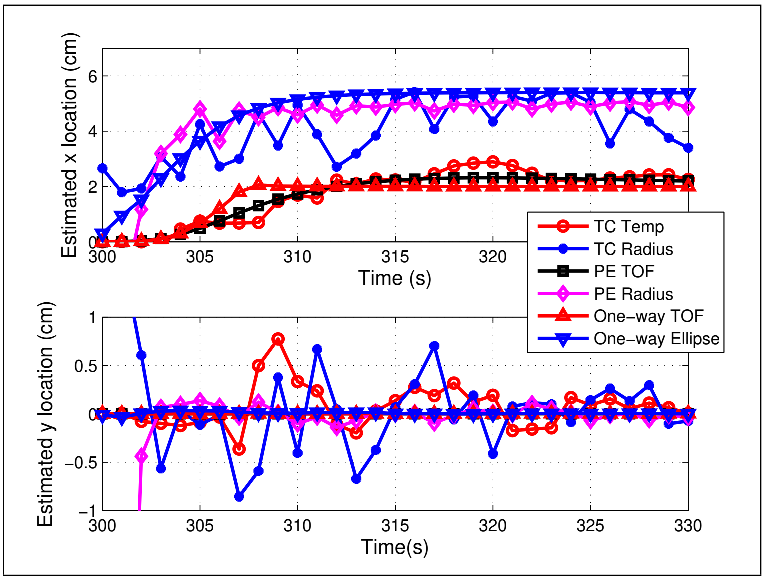

Figure 30: Extended Kalman filter convergence for all six measurement models with source at $(6cm,\ 0cm)$ and initial guess of $(0cm,\ 0cm)$.

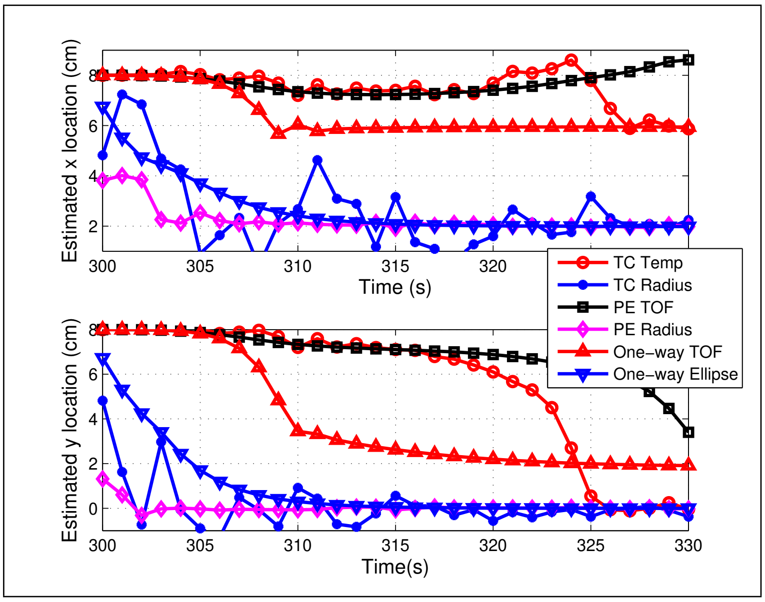

Figure 31: Extended Kalman filter convergence for all six measurement models with source at ($2cm$, $0cm$) and initial guess of ($8cm$, $8cm$).

sensor pair. More generally, the sensitivity is greater in the direction normal to the ultrasonic pulse propagation path.

The sensitivity to heating source location is expressed as

$$S_{xy} = \sqrt{\left(\frac{\partial \theta_{avg}}{\partial x}\right)^2 + \left(\frac{\partial \theta_{avg}}{\partial y}\right)^2}. \tag{41}$$

Figures 35 and 36 illustrate S_{xy} at two different times during the heating. These figures highlight the high sensitivity regions around the sensor path and the drastic drop-off near the path. These figures support the observation above that sensitivity is greater perpendicular to the ultrasonic propagation path. One should notice the rapid decrease in sensitivity as the source location nears the path between sensors.

5.2 Sensitivity to boundary conditions and thermal conductivity

Sensitivity to boundary conditions (Figure 18) and thermal conductivity are analyzed for an ultrasonic sensor configuration of four sensors in an $8cm$ square configuration (Figure 37). This configuration is based on the sensitivity analysis in Section 5 and represents a starting point for analysis. Sensitivity for the primary heat flux (q''), secondary heating magnitude and spread (q''_g and σ_g^2), convection coefficients for the plate (h_{sides} and h_{edges}), and thermal conductivity of the plate (k) are illustrated and analyzed for source locations inside the sensor grid and up to $2cm$ outside the grid (i.e., a $12cm$ by $12cm$ area).

Assumptions for the sensitivity to boundary conditions and thermal conductivity analysis are:

1. Source at known, fixed position

2. Source applied at time $t = 300s$ and removed at $t = 600s$

3. Main heat flux $q'' = 0.930MW/m^2$ over $0.00635m$ diameter circular area during heating (value obtained in previous study Myers et al. [2010a,b, 2012c])

4. Secondary heating is characterized by a Gaussian with magnitude $q''_g = 100W/m^2$ and variance $\sigma_g^2 = 0.0009m^2$ during heating

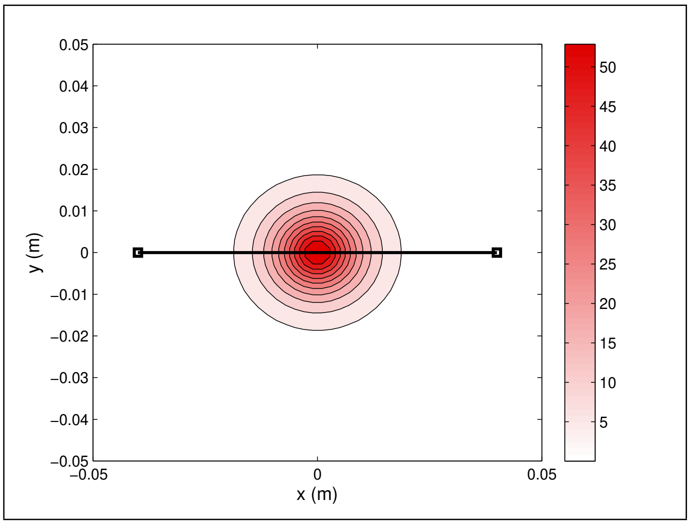

Figure 32: Temperature response at $t = 320s$ with source located at $(x = 0cm,\ y = 0cm)$. $\theta_{avg} = 13.5K$ between sensors.

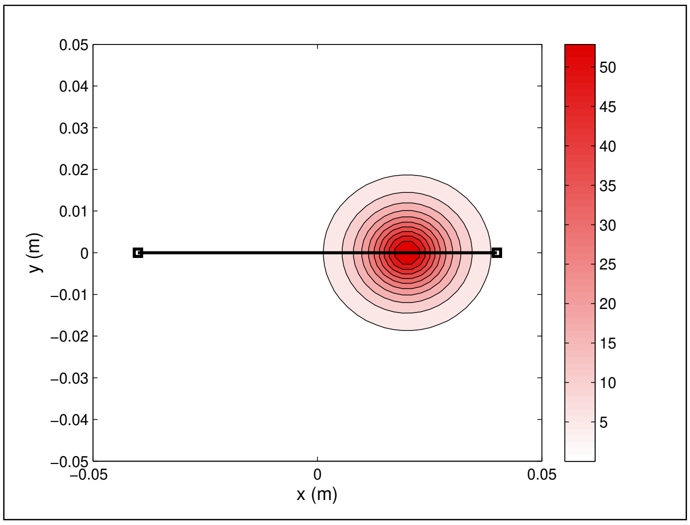

Figure 33: Temperature response at $t = 320s$ with source located at $(x = 2cm,\ y = 0cm)$. $\theta_{avg} = 13.2K$ between sensors.

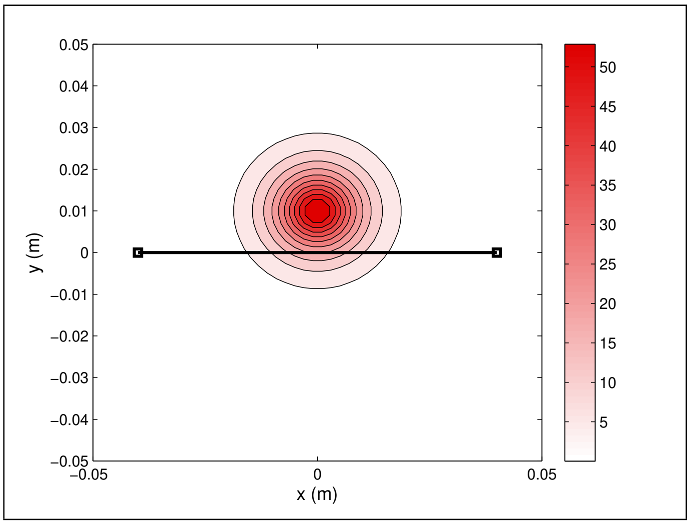

Figure 34: Temperature response at $t = 320s$ with source located at $(x = 0cm, y = 1cm)$. $\theta_{avg} = 5.3K$ between sensors.

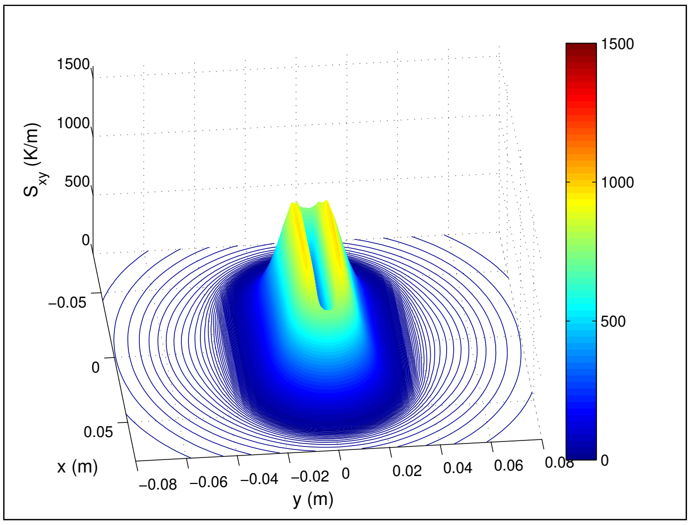

Figure 35: Heating source location sensitivity for one-way pulse sensor configuration and all possible heating source locations at t=320s.

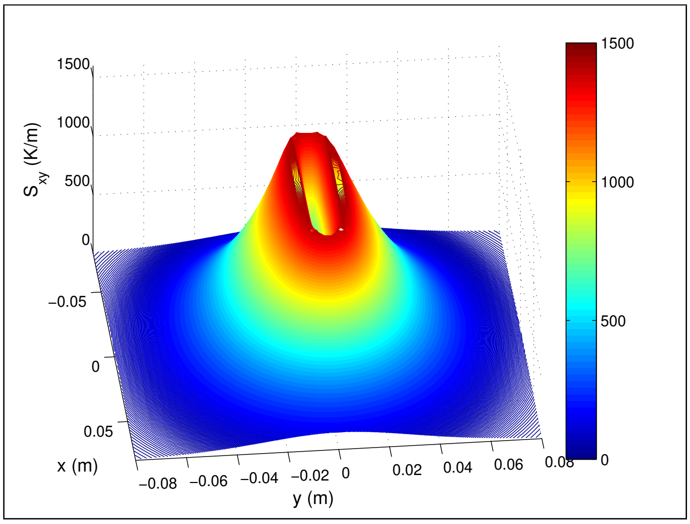

Figure 36: Heating source location sensitivity for one-way pulse sensor configuration and all possible source locations at $t = 450s$.

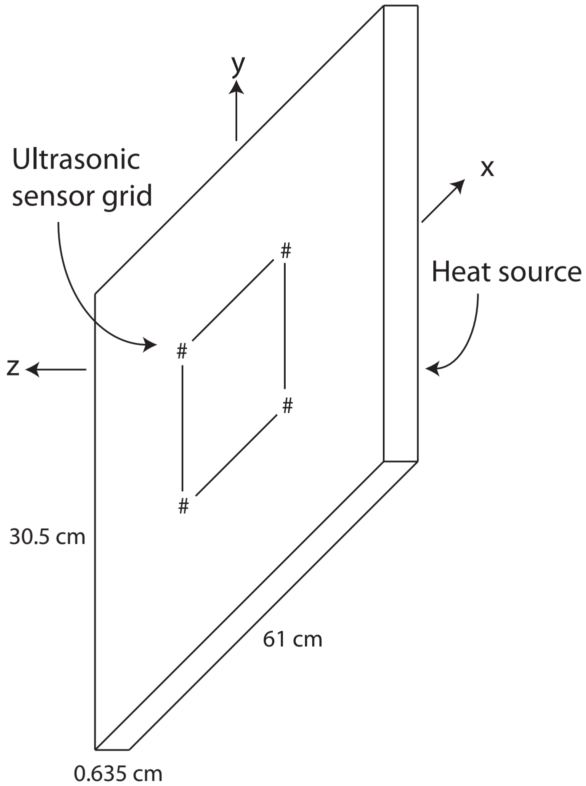

Figure 37: Ultrasonic sensor grid on the non-heated side of the plate with # symbols representing sensors and lines representing the ultrasonic pulse propagation paths between sensors (not drawn to scale).

5. Convection coefficient $h = 3.20W/m^2 - K$ on both sides of the plate (value obtained in previous study Myers et al. [2010a,b, 2012c])

6. Convection coefficient $h = 3W/m^2 - K$ on the plate edges

7. Thermal conductivity $k = 14.6W/m - K$

8. Specific heat $C_p = 500J/kgK$ and density $\rho = 8,000kg/m^3$

9. Positions of sensors are $(\pm 4cm, \pm 4cm)$ on the non-heated side

Sensitivity is computed using finite differences where baseline ultrasonic pulse time of flight values are computed using the assumptions above and then new ultrasonic pulse time of flight values are computed with the parameter being investigated multiplied by $1+\delta$. Sensitivities are presented scaled according to the relationBeck and Arnold [1977]

$$S_{\beta_i} = \beta_i \frac{\partial G}{\partial \beta_i} \tag{42}$$

$$S_{\beta_i} \approx \beta_i \frac{G(x, y, z, t, \beta_1, \cdots, \beta_i(1+\delta), \cdots, \beta_p) - G(x, y, z, t, \beta_1, \cdots, \beta_p)}{\beta_i(1+\delta) - \beta_i} \tag{43}$$

$$S_{\beta_i} \approx \frac{G(x, y, z, t, \beta_1, \cdots, \beta_i(1+\delta), \cdots, \beta_p) - G(x, y, z, t, \beta_1, \cdots, \beta_p)}{\delta} \tag{44}$$

where β_i is the parameter being investigated and G is ultrasonic pulse time of flight. The δ parameter used in this section is $\delta = 0.001$. By normalizing the sensitivities, direct comparison between all investigated parameters can be performed.

6 Comparison

The flat plate experiments detailed above are used in this section for comparing filter performance. This section examines heating source localization using four ultrasonic transducers in an $8cm$ square pattern (Figure 37).

Locating and characterizing a heating source depends upon many factors such as heating source movements in time, heating source magnitude changes in time, and other transient behaviors. Fairly restrictive assumptions can be imposed that simplify the problem. Analysis and algorithm development can proceed using these restrictive assumptions and then assumptions can be relaxed in stages to achieve the end result of source localization and characterization. The assumptions for this work are:

1. Source in fixed position (location unknown)

2. Source applied at time $t = 300s$ and removed at $t = 600s$

3. Main heat flux $q'' = 0.930MW/m^2$ over $0.00635m$ diameter circular area while source applied (value obtained in previous study Myers et al. [2010a,b, 2012c])

4. Secondary heating is characterized by a Gaussian with magnitude $q''_g = 100W/m^2$ and spread $\sigma_g^2 = 0.0009m^2$ while source applied

5. Convection coefficient $h = 3.20W/m^2K$ on both sides of the plate (value obtained in previous study Myers et al. [2010a,b, 2012c])

6. Convection coefficient $h = 3W/m^2K$ on the plate edges

7. Thermal conductivity $k = 14.6W/mK$

8. Specific heat $C_p = 500J/kgK$ and density $\rho = 8,000kg/m^3$

9. Positions of sensors are $(\pm 4cm, \pm 4cm)$ on the non-heated side

The three inverse methods compared are: extended Kalman filter, particle filter, and least squares. The two measurement models studied are: ultrasonic pulse one-way time of flight measurement model, and ellipse from ultrasonic pulse one-way time of flight measurement model. With the particle filter, only the ultrasonic pulse one-way time of flight measurement model is considered because, as will become clear later, the particle filter does not depend upon a Jacobian, and the ellipse model is an alternative way of expressing the Jacobian for those methods that require a Jacobian. Comparison of the five methods is performed in locating the heating source on the plate in the $x - y$ plane (x_q, y_q). For all methods, the state therefore is $X_t = [x_q, y_q]^T$. In all methods considered, the ultrasonic time of flight is normalized by the time of flight before the heating source is applied to the plate (G_{ij}/G_0).

6.1 Extended Kalman filter with ultrasonic pulse one-way time of flight measurement model

The extended Kalman filter algorithm to locate the source can be found in Table 2 . The state is $X_t = [x_q, y_q]^T$, and there is no input (U_t) to the state; thus the extended Kalman filter state model is $a = I_2$ and the state model Jacobian is $A = I_2$, where I_2 is a 2×2 identity matrix. A parameter sweep is conducted for the state model variance from $\sigma^2 = 0.01m^2$ to $\sigma^2 = 0.000001m^2$. A small value for the state model variance ($\sigma^2 = 0.000001m^2$) produces a damping effect on the convergence whereas a large value ($\sigma^2 = 0.01m^2$) produces fast but erratic convergence. From this parameter sweep, it is determined that a state variance of $\sigma^2 = 0.0001m^2$ provides a good compromise between damping and stability and this value is used. Thus, the state model covariance matrix is $Q_t = 0.0001m^2 \times I_2$.

This measurement model consists of obtaining expected temperatures from the direct model using the predicted state $\overline{X}_t$, computing the average temperature between the transducers, and then computing an expected time of flight from 29 to form $b(\overline{X}_t)$ (equation 45). For the current analysis, the average temperature is computed along the path on the non-heated plate surface between the two sensors. The Jacobian partial derivatives are obtained using finite difference when moving the source in the x and y directions independently (equation 46).

$$b(\overline{X}_t) = \begin{bmatrix} \overline{G}_1 \\ \overline{G}_2 \\ \overline{G}_3 \\ \overline{G}_4 \end{bmatrix}; \tag{45}$$

$$B_t = \begin{bmatrix} -\frac{\partial \overline{G}_1}{\partial x_1} & -\frac{\partial \overline{G}_1}{\partial y_1} \\ -\frac{\partial \overline{G}_2}{\partial x_2} & -\frac{\partial \overline{G}_2}{\partial y_2} \\ -\frac{\partial \overline{G}_3}{\partial x_3} & -\frac{\partial \overline{G}_3}{\partial y_3} \\ -\frac{\partial \overline{G}_4}{\partial x_4} & -\frac{\partial \overline{G}_4}{\partial y_4} \end{bmatrix}, \tag{46}$$

where t is time in seconds with a time step of $1s$, $\overline{G}_i$ with $i = 1, 2, 3, 4$ is the ultrasonic pulse time of flight with the heating source located at (x_s, y_s), and (x_i, y_i) with $i = 1, 2, 3, 4$ are the locations of four transducers. The Jacobian B_t is constructed using the derivatives with respect to sensor position for convenience because this information can be obtained with one direct model simulation. The derivatives are obtained from the direct model using finite differences by independently varying the x and y positions of all sensors by $0.0001m$. Based on the flat plate experiment above, the sensor noise is assumed be $\pm 6{-}5$ (a non-dimensional number based on G_{ij}/G_0) and is normally distributed ($\sigma^2 = ((6{-}5)/3)^2 = 4{-}10$). Solution instabilities were present when using this variance, which were reduced by increasing the variance to $4{-}7$. This larger variance effectively dampens the solution and prevents large changes from one iteration to the next. The measurement covariance matrix, therefore, is $R = 4{-}7 \times I_4$.

6.2 Extended Kalman filter with ellipse from ultrasonic pulse one-way time of flight measurement model

In an attempt to simplify the sensitivity calculation, the lines of constant time of flight around the sensor pairs form approximate ellipses. With this approximation, the sensitivities can be calculated algebraically. Figure 27 illustrates the geometry of an ellipse, where the two sensors are assumed to be the foci for the ellipse. Since the distance between sensors is known, ellipse parameters c and d can be related to each other and the ellipse can be represented with just one parameter c.

$$r_{is} + r_{js} = 2c = \sqrt{r_{ij}^2 + 4d^2} \tag{47}$$

where i and j are sensors and s is heat source.

$$c = \frac{1}{2}\sqrt{r_{ij}^2 + 4d^2} = \frac{r_{is} + r_{js}}{2} \tag{48}$$

$$r_{is} = \sqrt{(x_i - x_s)^2 + (y_i - y_s)^2} \tag{49}$$

$$r_{js} = \sqrt{(x_j - x_s)^2 + (y_j - y_s)^2} \tag{50}$$

$$\frac{\partial c_i}{\partial x_s} = \frac{1}{2}\left[\frac{x_s - x_i}{r_{is}} + \frac{x_s - x_j}{r_{js}}\right] \tag{51}$$

$$\frac{\partial c_i}{\partial y_s} = \frac{1}{2}\left[\frac{y_s - y_i}{r_{is}} + \frac{y_s - y_j}{r_{js}}\right] \tag{52}$$

This measurement model consists of measuring the one-way ultrasonic pulse time of flight, using the direct model to obtain the average temperature between the transducers for a range of c values, using equation 29 to compute time of flight for the range of c values, and then interpolating the time of flight results using the spline method to obtain c for the measured time of flight. The measurement transition function $b(\overline{X}_t)$ and the Jacobian B_t are then

$$b(\overline{X}_t) = \begin{bmatrix} c_1 \\ c_2 \\ c_3 \\ c_4 \end{bmatrix}; \tag{53}$$

$$B_t = \begin{bmatrix} \frac{\partial c_1}{\partial x_s} & \frac{\partial c_1}{\partial y_s} \\ \frac{\partial c_2}{\partial x_s} & \frac{\partial c_2}{\partial y_s} \\ \frac{\partial c_3}{\partial x_s} & \frac{\partial c_3}{\partial y_s} \\ \frac{\partial c_4}{\partial x_s} & \frac{\partial c_4}{\partial y_s} \end{bmatrix}, \tag{54}$$

where t is time in seconds with a time step of 1 second, c_i with $i = 1, 2, 3, 4$ is the ellipse parameter if the source is located at (x_s, y_s). Based on the flat plate experiment above, sensor noise is assumed be $\pm 1.05{-}8s$ and is normally distributed ($\sigma^2 = 1.22{-}17sec^2$). The sensor noise in terms of temperature can be expressed as

$$\theta_{noise} = \frac{G_{noise} v_0}{L\xi} = 6.09K \tag{55}$$

Using the average slope of $0.015m/K$ determined in Section 4 and documented in previous work Myers et al. [2010a,b, 2012c], ellipse noise for the c parameter from ultrasonic pulse time of flight measurement model is $\pm 0.0914m$ and is normally distributed ($\sigma^2 = 9.28{-}4m^2$). Since the measurement covariance matrix R represents the measurement noise of the c parameter, the measurement covariance is $3.19{-}10m^2$ ($[1.05{-}8s/3 \times 5, 100m/sec$ sound speed$]^2$).

6.3 Particle filter with ultrasonic pulse one-way time of flight measurement model

The particle filter is an alternative nonparametric implementation of the Bayes filter and is a Monte Carlo technique used for the solution of state estimation problems. The main idea is to represent the required posterior density function by a set of random samples with associated weights and to compute the estimates based on these samples and weights Vianna et al. [2010]. Because it is nonparametric, the particle filter can represent a much broader space of distributions than Gaussians and has the ability to model nonlinear transformations of random variables Thrun et al. [2006]. The particle filter algorithm to locate the source can be found in Table 5.

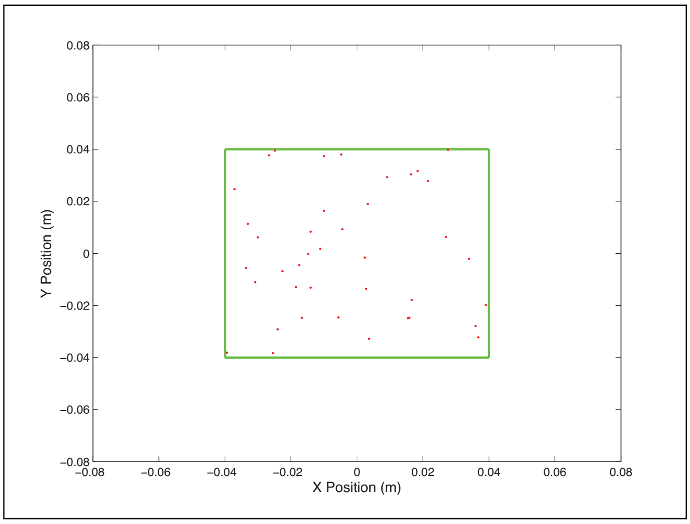

Figure 38: Particle locations ($m = 40$) at $300s$.

Implementation of the particle filter for heating source localization starts with defining the area of possible source locations on the plate. The number of particles m to use in the algorithm must also be defined. A large number of particles yields a higher probability that one or more particles will be located near the actual source but the downside is higher computational cost. For this study, the area is defined as the $8cm \times 8cm$ sensor grid and the number of particles is $m = 40$. The algorithm starts with the generation of m random particles within the defined area of possible source locations (Figure 38). Step 2 involves obtaining expected temperatures from the direct model with the heating source at each particle location, computing the average temperature between the transducers, and then computing an expected time of flight to form $Z_{i,t}$, a 4×1 matrix for each particle i at the current time t. For the current analysis, the average temperature is computed along the path on the non-heated plate surface between the two sensors. Step 3 entails obtaining actual ultrasonic time of flight measurements at the current time t for all four sensor pairs to form $Ztrue_t$, a 4×1 matrix. The particle filter relies on an importance factor, or weight $w_{i,t}$, to incorporate the measurement $Ztrue_t$ into the particle set. The weight $w_{i,t}$ for each particle is computed in Step 4 using

$$\begin{aligned} w_{i,t} &= N(Ztrue_t, I) \\ &= det(2\pi I)^{-\frac{1}{2}} exp\left\{-\frac{1}{2}((Z_{i,t} - Ztrue_t) \times gain)^T I^{-1}((Z_{i,t} - Ztrue_t) \times gain)\right\}. \end{aligned} \tag{56}$$

Gain is discussed in detail later in this section. A number of resampling techniques have been devised Thrun et al. [2006], Vianna et al. [2009], Arulampalam et al. [2002]. This work employs the sampling importance resampling technique because this technique requires fewer particles than some of the other methods and focuses the computational resources to regions in the state space with high posterior probability Thrun et al. [2006]. In Step 5, the particle weights are normalized into bins from 0 to 1, which gives the particles with the highest weight the largest bins and then in Step 6, the particles are resampled using a normal distribution. By resampling across the bins from 0 to 1 using a normal distribution, a higher probability exists that the best particles will be chosen but some particles that are not the best will be chosen too. It is important to note that the number of particles m remains constant through the resampling process, thus some particles will have identical locations on the plate after resampling. Degeneracy is common with particle filters, a situation where the solution converges to the one best particle within the current particle set without considering locations nearby Doucet et al. [2002]. This fact necessitates Step 7 where position noise or roughness is added to each particle Salmond et al. [1993]. In this work, uniform position noise of $\pm 0.5cm$ is used. Figures 39 and 40 illustrate the particle distribution before and after adding noise to each particle location. After completion of Step 7, the algorithm returns to Step 2 and the process is repeated for the next step in time. For this work, a time step of $1s$ is used. Figure 41 illustrates the particle distribution at $t = 330sec$.

Because the magnitude of the non-dimensional values in the matrix $Z_{i,t} - Ztrue_t$ in equation 56 ranges

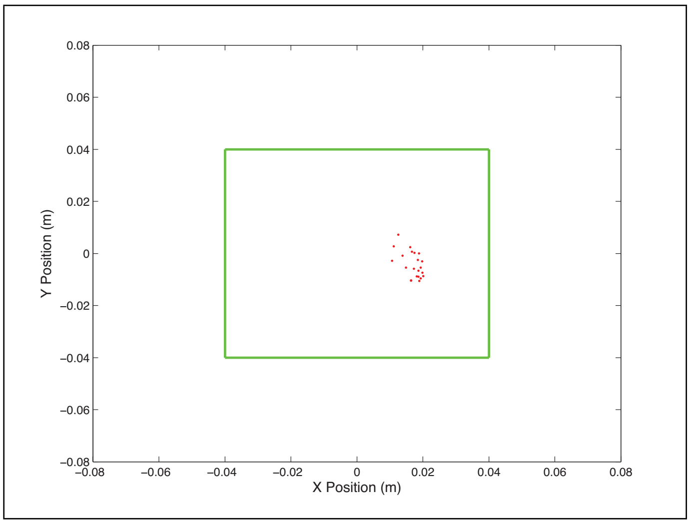

Figure 39: Particle locations ($m = 40$) at $315s$.

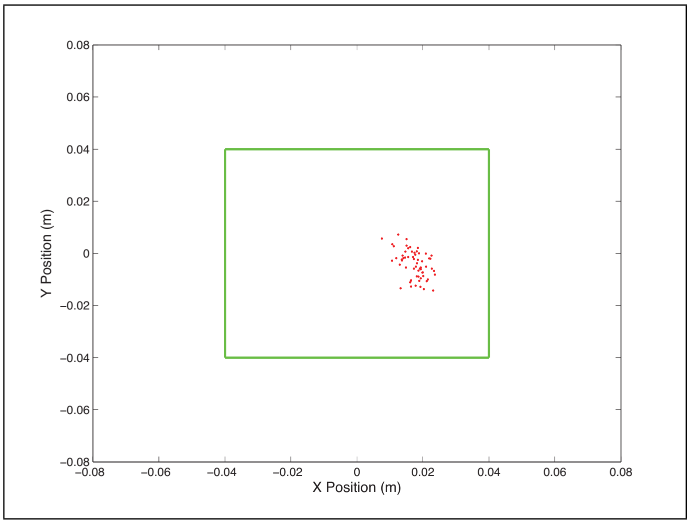

Figure 40: Particle locations ($m = 40$) at $315s$ after adding noise to each particle location.

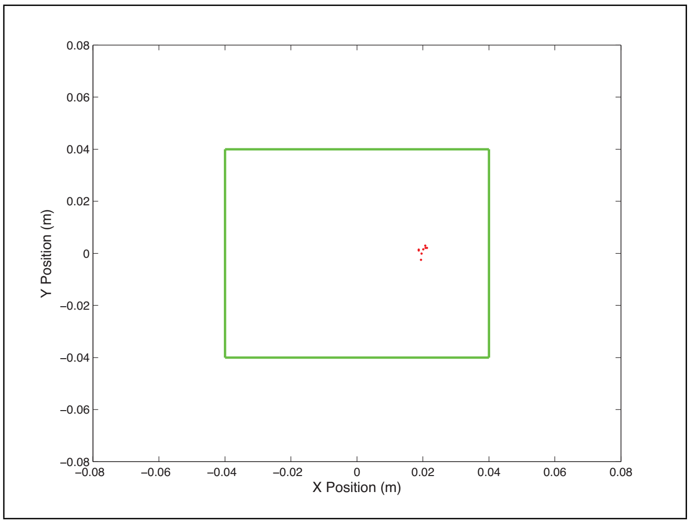

Figure 41: Particle locations ($m = 40$) at $330s$.

from 0 to 0.008, using no *gain* ($gain = 1$) produces a value of 1 in the exponent portion of the equation for all particles. Thus, identical weights are computed for all particles (Figure 42). For the particle filter to function properly, it is imperative that the particles close to the actual heating source location receive the highest weight ($Z_{i,t} - Ztrue_t$ close to zero in Figure 42) and those particles far from the actual heating source location receive a weight close to zero. The non-dimensional sensor noise measured in the experiment above is approximately 6−5. Therefore, the applied gain should yield the largest weights for $Z_{i,t} - Ztrue_t$ magnitudes between 0 and the noise of 6−5 and should yield weights close to 0 for $Z_{i,t} - Ztrue_t$ magnitudes larger than the sensor noise. Illustrated in Figure 42, a gain of 14 is too small to produce weights close to zero for $Z_{i,t} - Ztrue_t$ magnitudes larger than the sensor noise, but a gain of 64 precipitates the desired effect. Figure 43 illustrates the effect of the number of particles m on the convergence behavior and performance of the particle filter. The filter is quite robust and Figure 43 demonstrates the filter's ability to converge to the correct location with only 10 particles. The particle filter used in the comparisons with the other localization methods in the next section is based on 40 particles.

6.4 Least squares with ultrasonic pulse one-way time of flight measurement model

The ordinary least squares method is sometimes called the ÃGauss method of minimizationÃ Woodbury [2003a]. For the current localization, the estimated time of flight G for each sensor pair for a particular time t, a 4×1 matrix, depends on a vector of two unknowns in the state X and the value of G at $X = X + \Delta X$ is obtained through the truncated Taylor's series as

$$G|_{X+\Delta X} \approx G|_X + \left.\frac{\partial G}{\partial X}\right|_X \Delta X. \tag{57}$$

The derivative in equation 57 is the 4×2 sensitivity matrix

$$B_t = \frac{\partial G}{\partial X} = \begin{bmatrix} \frac{\partial \overline{G}_1}{\partial x_1} & \frac{\partial \overline{G}_1}{\partial y_1} \\ \frac{\partial \overline{G}_2}{\partial x_2} & \frac{\partial \overline{G}_2}{\partial y_2} \\ \frac{\partial \overline{G}_3}{\partial x_3} & \frac{\partial \overline{G}_3}{\partial y_3} \\ \frac{\partial \overline{G}_4}{\partial x_4} & \frac{\partial \overline{G}_4}{\partial y_4} \end{bmatrix} \tag{58}$$

where t is time in seconds with a time step of $1s$, $\overline{G}_i$ with $i = 1, 2, 3, 4$ is the ultrasonic pulse time of flight with the heating source located at (x_s, y_s), and (x_i, y_i) with $i = 1, 2, 3, 4$ are the locations of four transducers. The experimentally obtained time of flight measurements are designated as Z_t, a 4×1 matrix. The desire is

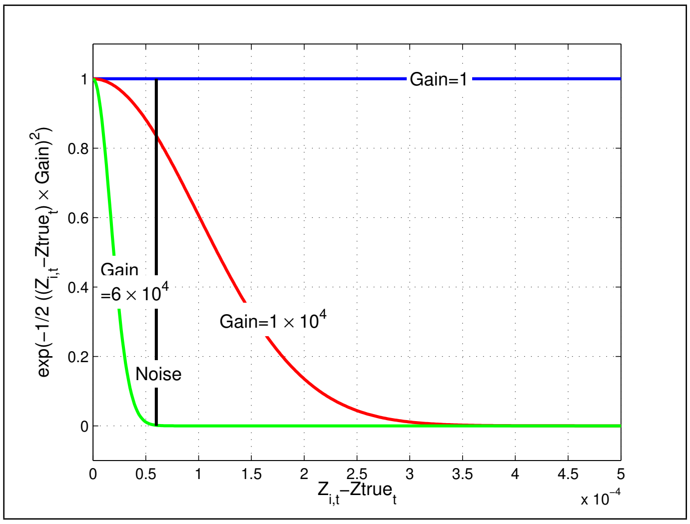

Figure 42: Comparison of selected particle filter gain values with sensor noise.

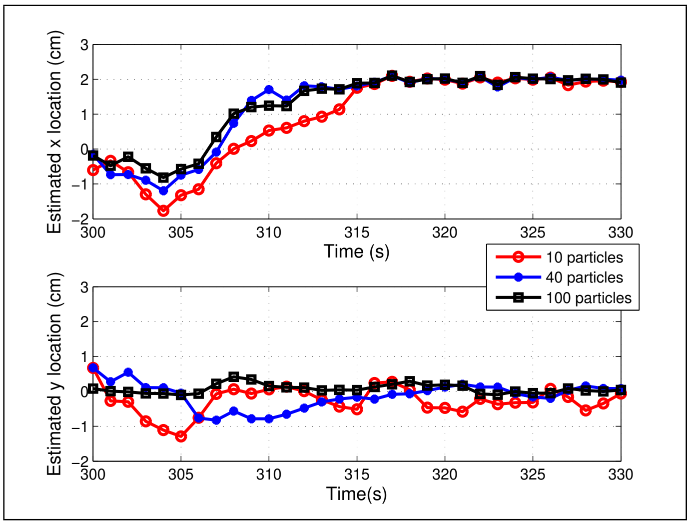

Figure 43: Particle filter convergence for selected numbers of particles with heating source located at $(x = 2cm,\ y = 0cm)$ and an initial guess of $(x = 0cm,\ y = 0cm)$.

to improve the estimate for the state X_t based on the observations Z_t. The ordinary least squares objective function is

$$S = (Z_t - G|_{X_t} - B_t \Delta X_t)^T (Z_t - G|_{X_t} - B_t \Delta X). \tag{59}$$

The minimizer of equation 59 is found by forcing to zero the derivative with respect to ΔX resulting in the estimator

$$\Delta X_t = (B_t^{\mathrm{T}} B_t)^{-1} B_t^{\mathrm{T}} (Z_t - G_t|_{X_t}). \tag{60}$$

This method consists of obtaining expected temperatures from the direct model, computing the average temperature between the transducers, and then computing an expected time of flight from equation 29. For the current analysis, the average temperature is computed along the path on the non-heated plate surface between the two sensors. The Jacobian B_t is constructed using the derivatives with respect to sensor position for convenience since this information can be obtained with one direct model simulation. The derivatives are obtained from the direct model using finite differences by independently varying the x and y positions of all sensors by $0.0001m$.

6.5 Least squares with ellipse from ultrasonic pulse one-way time of flight measurement model

This method uses the same ellipse model detailed above with the extended Kalman filter and employs least squares method detailed above to locate the source. Figure 27 illustrates the geometry of an ellipse, where the two sensors are assumed to be the foci for the ellipse. Since the distance between sensors is known, ellipse parameters c and d can be related to each other and the ellipse can be represented with just one parameter c.

$$r_{is} + r_{js} = 2c = \sqrt{r_{ij}^2 + 4d^2} \tag{61}$$

where i and j are sensors and s is heat source.

$$c = \frac{1}{2}\sqrt{r_{ij}^2 + 4d^2} = \frac{r_{is} + r_{js}}{2} \tag{62}$$

$$r_{is} = \sqrt{(x_i - x_s)^2 + (y_i - y_s)^2} \tag{63}$$

$$r_{js} = \sqrt{(x_j - x_s)^2 + (y_j - y_s)^2} \tag{64}$$

$$\frac{\partial c_i}{\partial x_s} = \frac{1}{2}\left[\frac{x_s - x_i}{r_{is}} + \frac{x_s - x_j}{r_{js}}\right] \tag{65}$$

$$\frac{\partial c_i}{\partial y_s} = \frac{1}{2}\left[\frac{y_s - y_i}{r_{is}} + \frac{y_s - y_j}{r_{js}}\right] \tag{66}$$

This measurement model consists of measuring the one-way ultrasonic pulse time of flight, using the direct model to obtain the average temperature between the transducers for a range of c values, using equation 29 to compute time of flight for the range of c values, and then interpolating the time of flight results using the spline method to obtain c for the measured time of flight. The sensitivity matrix B_t is then

$$B_t = \begin{bmatrix} \frac{\partial c_1}{\partial x_s} & \frac{\partial c_1}{\partial y_s} \\ \frac{\partial c_2}{\partial x_s} & \frac{\partial c_2}{\partial y_s} \\ \frac{\partial c_3}{\partial x_s} & \frac{\partial c_3}{\partial y_s} \\ \frac{\partial c_4}{\partial x_s} & \frac{\partial c_4}{\partial y_s} \end{bmatrix}, \tag{67}$$

where t is time in seconds with a time step of $1 second$, c_i with $i = 1, 2, 3, 4$ is the ellipse parameter if the source is located at (x_s, y_s). The desire is to improve the estimate for the state X_t based on the observations c.

6.6 Results

Convergence behavior for the three inverse methods and both measurement models is compared in Figures 44 through 46. With the heating source located inside the sensor grid (Figure 44), the extended Kalman filter

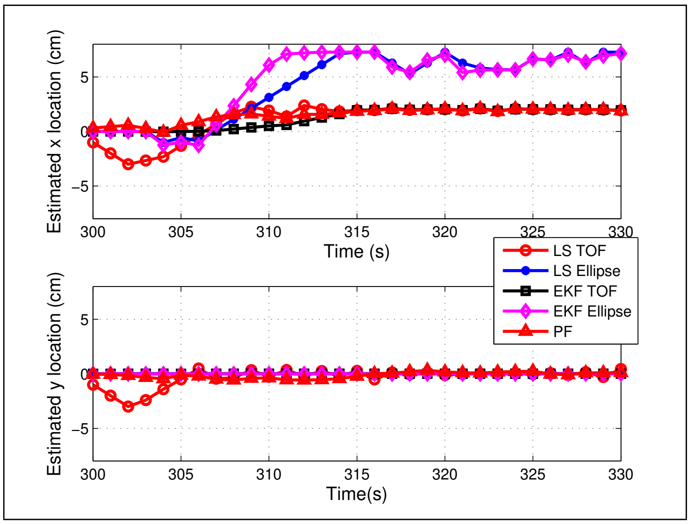

Figure 44: Least squares, extended Kalman filter, and particle filter convergence for both one-way ultrasonic pulse measurement models with the heating source located at $(x = 2cm,\ y = 0cm)$ and an initial guess of $(x = 0cm,\ y = 0cm)$.

and the least squares with the direct model and the particle filter converge to the correct location while the extended Kalman filter and the least squares with the ellipse model do not. Similar convergence behavior is found with the heating source located at the edge of the sensor grid (Figure 45), although convergence is much faster. With the heating source located outside of the sensor grid (Figure 46), none of the methods converge to the correct location. These examples started with an initial guess of $(x = 0cm,\ y = 0cm)$ for the heating source location.

Sensitivity to heating source location, explored in Section 5 and documented in previous work Myers et al. [2012b], can help explain these results. With the heating source outside the sensor grid, only one sensor pair would have sufficient sensitivity to heating source location and only then if the heating source is located close to the sensor pair. With only one sensor pair receiving usable information, the inverse routine has insufficient information to converge on the correct heating source location. With the heating source located inside the sensor grid, all sensor pairs receive usable information and the inverse routine is able to converge to the correct location. With the heating source located at the edge of the sensor grid, one sensor pair receives usable information almost instantaneously resulting in faster convergence.

The extended Kalman filter with ellipse and least squares with ellipse models use the least amount of wall time and but the most memory of the five methods. Wall time for each iteration, independent of re-computing the direct model for the updated parameters, is approximately three times longer for the least squares time of flight model and almost four times longer for the extended Kalman filter time of flight model than the wall time for both of the ellipse models. The particle filter requires approximately 37 times more wall time than the ellipse models. Memory usage is lowest for the extended Kalman filter time of flight model and the least squares time of flight model. The particle filter requires approximately 30% more memory and the ellipse models require approximately four times more memory than the time of flight models.

Repeating the experiment using multiplexing equipment and a complete sensor grid of four transducers instead of simulating the sensor grid with separate experiments using two transducers might produce different convergence behavior, especially for heating source locations outside the sensor grid. While the experiment is reproducible, simulating a sensor grid with separate experiments introduces uncertainties that could effect the results. Additionally, sensor and heating source placement introduce uncertainties when simulating the sensor grid.

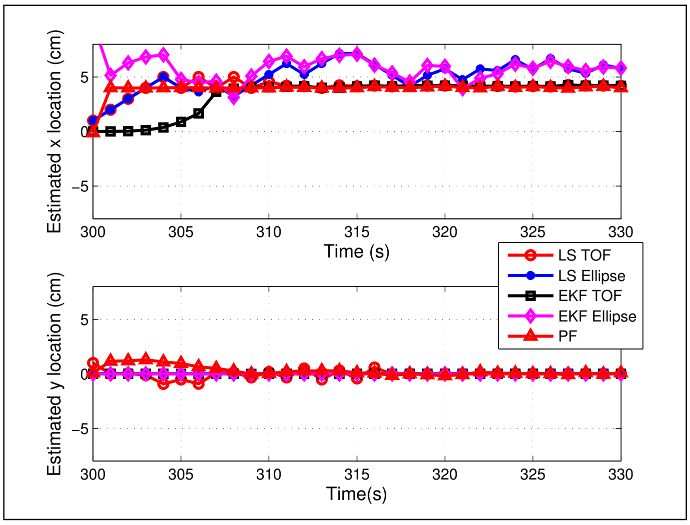

Figure 45: Least squares, extended Kalman filter, and particle filter convergence for both one-way ultrasonic pulse measurement models with the heating source located at $(x = 4cm,\ y = 0cm)$ and an initial guess of $(x = 0cm,\ y = 0cm)$.

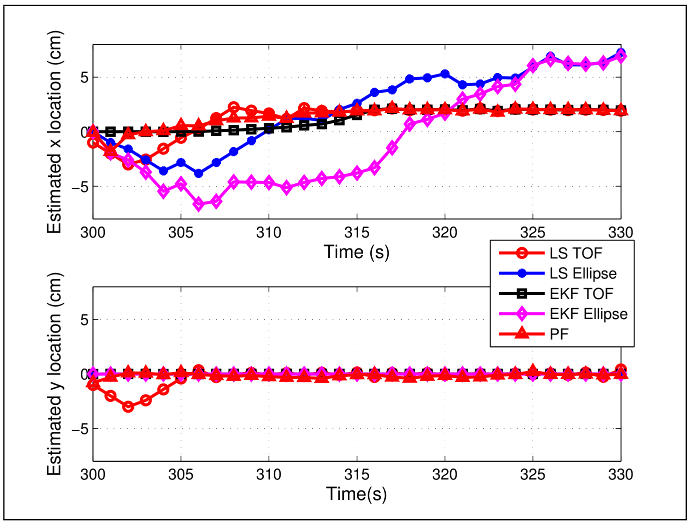

Figure 46: Least squares, extended Kalman filter, and particle filter convergence for both one-way ultrasonic pulse measurement models with the heating source located at $(x = 6cm,\ y = 0cm)$ and an initial guess of $(x = 0cm,\ y = 0cm)$.

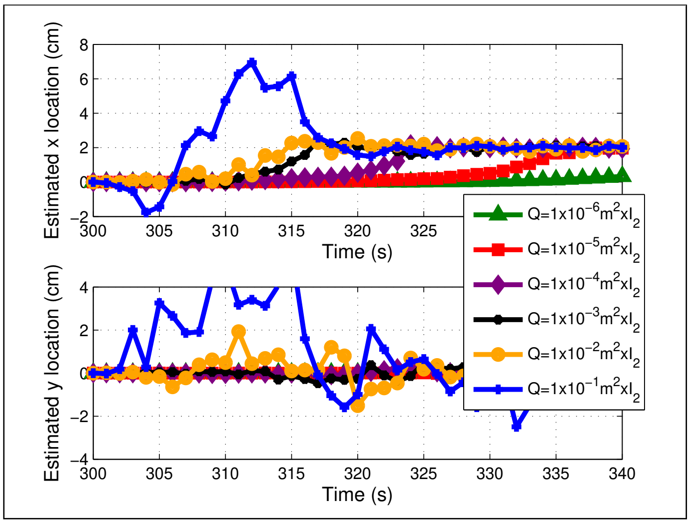

Figure 47: Extended Kalman filter convergence for a range of state model covariance values (Q) with constant measurement covariance values of $R = 4{-}7 \times I_4$, the heating source located at $(x = 2cm,\ y = 0cm)$, and an initial guess of $(x = 0cm,\ y = 0cm)$.

6.7 Adaptive extended Kalman filter

Figure 47 illustrates the sensitivity to the state model covariance by comparing values from $Q = 0.1m^2 \times I_2$ to $0.000001m^2 \times I_2$. Decreasing the state model covariance (Q) magnitude results in a damping effect on the convergence. Decreasing the magnitude too far causes the estimated position values to remain fairly constant and the solution fails to converge. Conversely, increasing the state model covariance (Q) magnitude increases the convergence rate. Increasing the state model covariance (Q) too far results in erratic position estimates and the solution fails to converge.

Figure 48 illustrates the sensitivity to the measurement covariance by comparing values from $R = 4{-}5 \times I_4$ to $R = 4{-}10 \times I_4$. Increasing the measurement covariance (R) magnitude results in a damping effect on the convergence. Increasing the magnitude too far causes the estimated position values to remain fairly constant and the solution fails to converge. Conversely, decreasing the measurement covariance (R) magnitude increases the convergence rate. Decreasing the measurement covariance (R) too far results in erratic position estimates and the solution fails to converge.

A trend is evident when comparing Figures 47 and 48 in that Q and R appear to be inversely correlated. Figure 49 illustrates the relationship. Decreasing Q by one order of magnitude or increasing R by one order of magnitude results in similar convergence behavior. Likewise, increasing Q by one order of magnitude or decreasing R by one order of magnitude also results in similar convergence behavior. For example, using $Q = 0.0001m^2 \times I_2$ and $R = 4{-}7 \times I_4$ as the baseline, decreasing the state model covariance to $Q = 0.00001m^2 \times I_2$ but keeping the measurement covariance at $R = 4{-}7 \times I_4$ results in similar convergence behavior if the state model covariance is kept at $Q = 0.0001m^2 \times I_2$ and the measurement covariance is increased to $R = 4{-}6 \times I_4$.

We can conclude from these observations that the state model covariance (Q) and the measurement covariance (R) are correlated for this heating source localization scenario. The measurement covariance is determined from sensor noise, a measurable quantity, and the state model covariance is unknown and not measurable. Therefore, a large uncertainty exists in the state model covariance while a small uncertainty exists in the measurement covariance. Selection of an appropriate state model covariance must then be obtained through a parameter sweep while observing convergence behavior.

Figure 51 illustrates the magnitude of each element in the Kalman gain (K_t), which, for this heating source localization, is a 2×4 matrix. Comparing Figure 51 with Figure 50, the $(1, 3)$ value from the Kalman gain (K_t) stands out as a possible source since it increases until convergence and then decreases rapidly. However, this value remains large even after convergence.

Figure 52 illustrates the normalized magnitude of the variance contained in the state covariance matrix (Σ) which is a 2×2 matrix in this heating source localization problem. The variance values are in the main diagonal

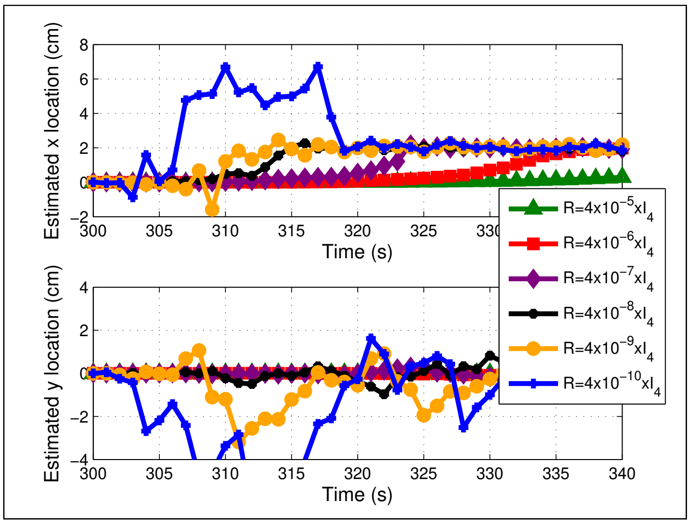

Figure 48: Extended Kalman filter convergence for a range of measurement covariance values (R) with constant state model covariance values of $Q = 1{-}4m^2 \times I_2$, the heating source located at ($x = 2cm$, $y = 0cm$), and an initial guess of ($x = 0cm$, $y = 0cm$).

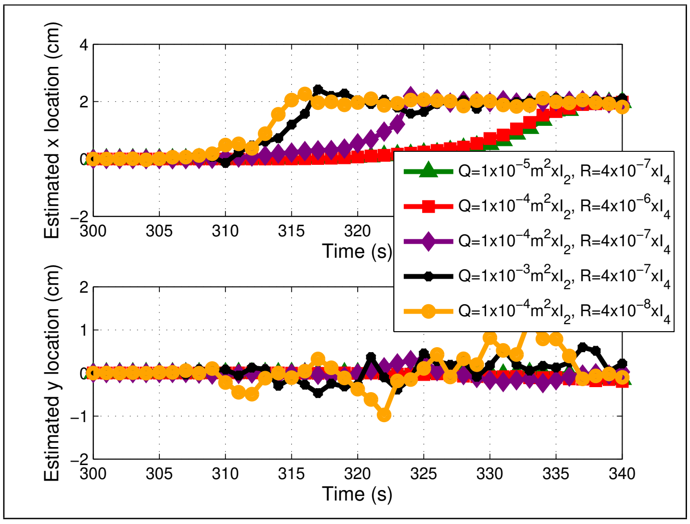

Figure 49: Extended Kalman filter convergence illustrating the correlation between the state model covariance matrix (Q) and the measurement covariance matrix (R). The heating source is located at ($x = 2cm$, $y = 0cm$) with an initial guess of ($x = 0cm$, $y = 0cm$).

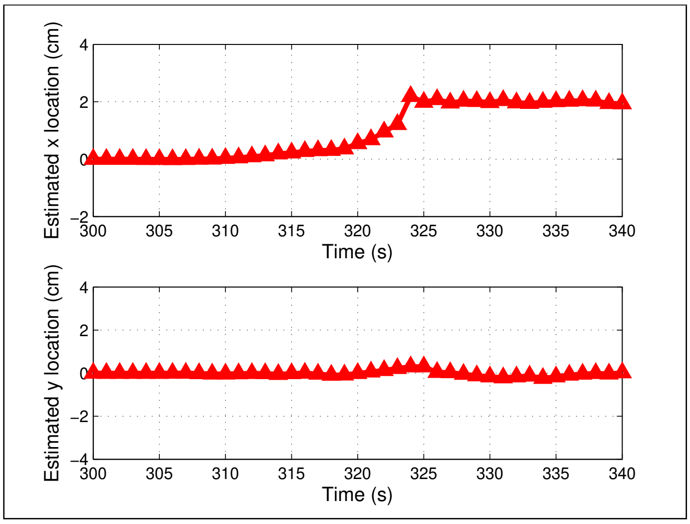

Figure 50: Extended Kalman filter convergence with the state model covariance values of $Q = 1{-}4m^2 \times I_2$, measurement covariance values of $R = 4{-}7 \times I_4$, heating source located at ($x = 2cm$, $y = 0cm$), and an initial guess of ($x = 0cm$, $y = 0cm$).

of the matrix and are identical. Comparing with Figure 50, we observe that the variance increases steadily, decreases rapidly just before and during convergence, and remains small after convergence. Figure 53 illustrates the normalized magnitude of the variance for a range of state model covariance values from $Q = 1{-}1m^2 \times I_2$ to $Q = 1{-}6m^2 \times I_2$ and a measurement covariance of $R = 4{-}7 \times I_4$. A comparison of Figure 53 with Figure 47 yields the observation that the variance increases steadily, decreases rapidly just before and during convergence, and remains small after convergence for every state model covariance examined.

The adaptive extended Kalman filter incorporates three new parameters. The predefined tolerance value $\Sigma_{tolerance}$ for changes to the state covariance Σ is based on the variance found in the first iteration and is defined as $\Sigma_{tolerance} = \Sigma_1$. The magnitude of Σ is dependent upon filter parameters including the state model covariance Q, thus basing the tolerance on the first iteration ensures the adaptive nature of the filter will smooth convergence near the converged solution. The predefined limit to convergence rate ΔX_{limit} for this work is defined as $\Delta X_{limit} = [\Delta x_{limit}, \Delta y_{limit}]^T = [1cm/sec, 1cm/sec]^T$. Figure 54 illustrates convergence for the adaptive extended Kalman filter with $Q_0 = 1{-}4m^2 \times I_2$, $R = 4{-}7 \times I_4$, and an adaptive gain of $M_t = 2$. The adaptive extended Kalman filter outperforms the extended Kalman filter in this example. Figure 55 illustrates the variance value in Q during convergence for the adaptive extended Kalman filter while Figure 56 illustrates the variance values from Σ for a range of initial state model covariance Q_0 values.

Figure 57 illustrates the effect that different initial state model covariance values has on the adaptive extended Kalman filter convergence. Comparing with Figure 47, the adaptive extended Kalman filter is able to converge quicker for a significant range of initial state model covariance values Q_0. Figure 58 illustrates the sensitivity to the adaptive extended Kalman filter gain M_t.

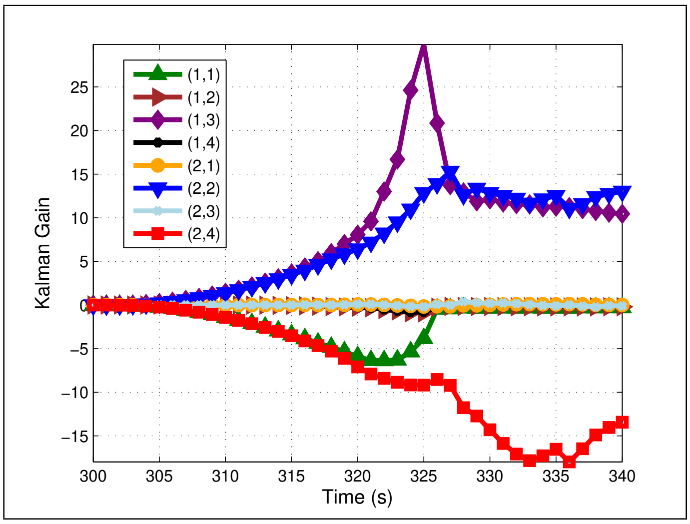

Figure 51: Kalman gain values during convergence for state model covariance of $Q = 1{-}4m^2 \times I_2$ and measurement covariance of $R = 4{-}7 \times I_4$. The heating source is located at $(x = 2cm,\ y = 0cm)$ with an initial guess of $(x = 0cm,\ y = 0cm)$. Legend entries refer to the matrix element in the Kalman gain which is a 2×4 matrix. Convergence (from Figure 50) is at $324s$.

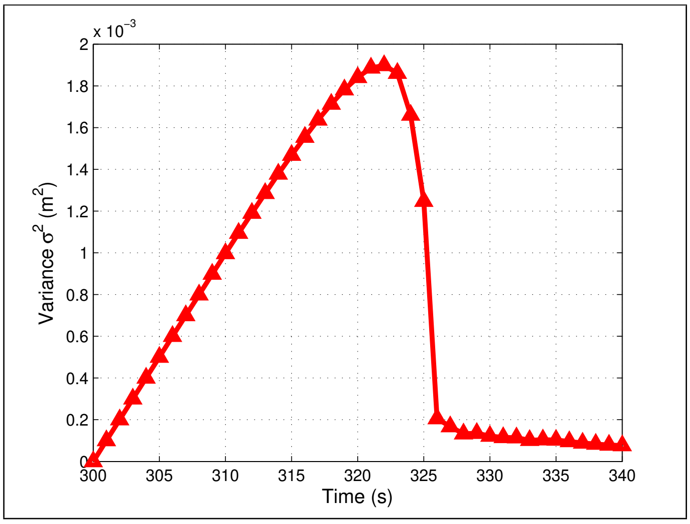

Figure 52: Variance (σ^2) from the state covariance matrix (Σ) for state model covariance of $Q = 1{-}4m^2 \times I_2$ and measurement covariance of $R = 4{-}7 \times I_4$. The heating source is located at $(x = 2cm,\ y = 0cm)$ with an initial guess of $(x = 0cm,\ y = 0cm)$. Convergence (from Figure 50) is at $324s$.

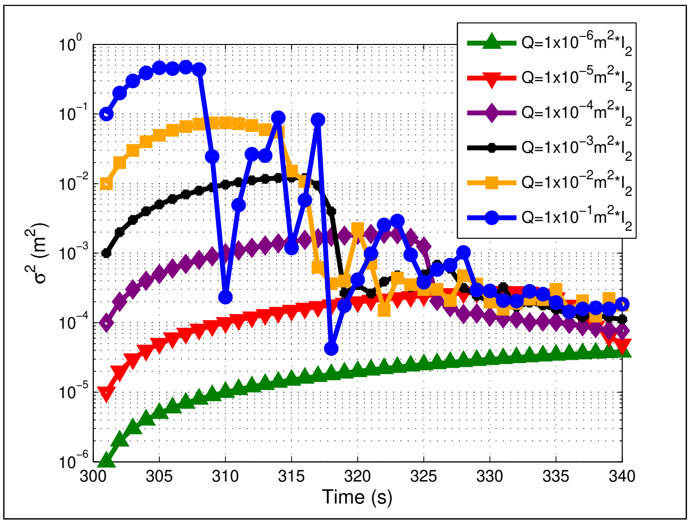

Figure 53: Variance (σ^2) from the state covariance matrix (Σ) for a range of state model covariance values (Q) and constant measurement covariance of $R = 4{-}7 \times I_4$. The heating source is located at ($x = 2cm$, $y = 0cm$) with an initial guess of ($x = 0cm$, $y = 0cm$). Convergence behavior can be found in Figure 47.

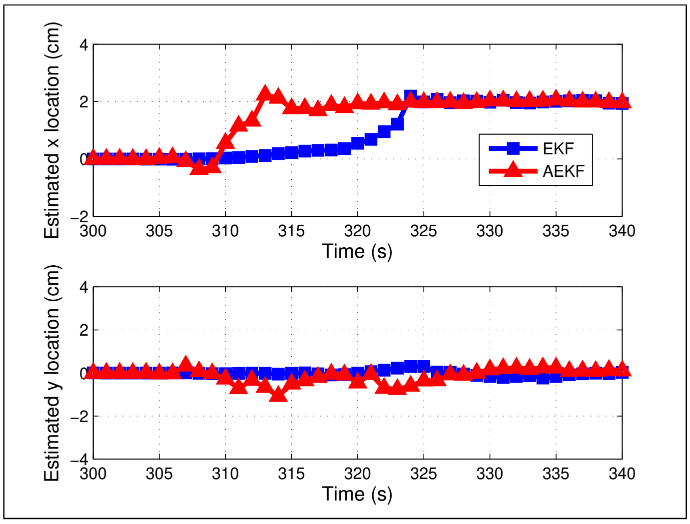

Figure 54: Extended Kalman filter and adaptive extended Kalman filter convergence with $Q_0 = 1{-}4m^2 \times I_2$, $R = 4{-}7 \times I_4$, and $M = 2$. The heating source is located at ($x = 2cm$, $y = 0cm$) with an initial guess of ($x = 0cm$, $y = 0cm$).

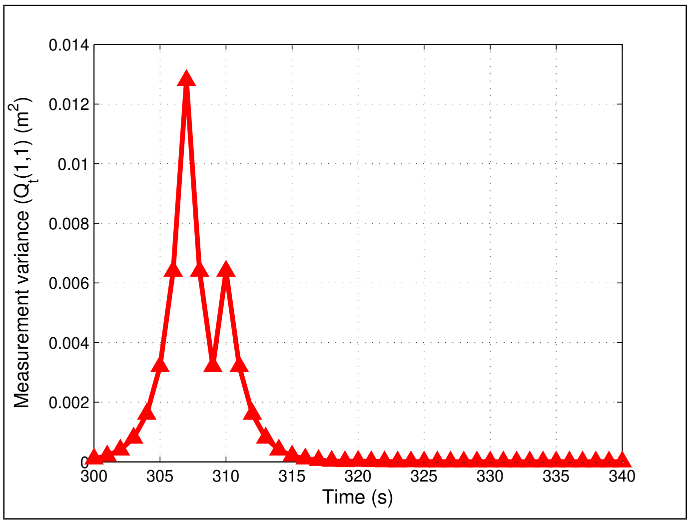

Figure 55: Adaptive extended Kalman measurement covariance (Q_t) values during convergence with $Q_0 = 1{-}4m^2 \times I_2$, $R = 4{-}7 \times I_4$, and $M_t = 2$. The heating source is located at ($x = 2cm$, $y = 0cm$) with an initial guess of ($x = 0cm$, $y = 0cm$).

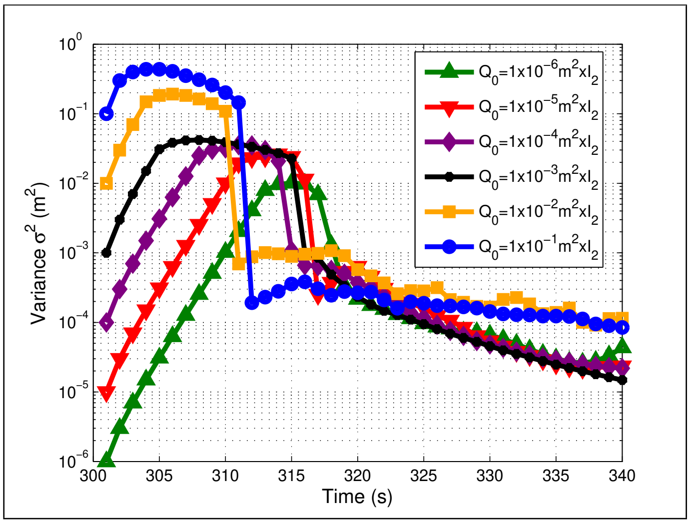

Figure 56: Adaptive extended Kalman filter variance (σ^2) from the state covariance matrix (Σ) for a range of starting state model covariance values (Q_0), constant measurement covariance of $R = 4{-}7 \times I_4$, and $M_t = 2$. The heating source is located at ($x = 2cm$, $y = 0cm$) with an initial guess of ($x = 0cm$, $y = 0cm$).

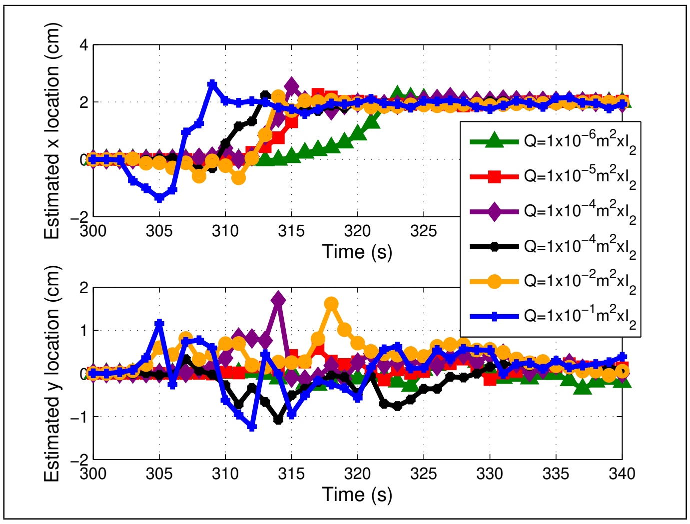

Figure 57: Adaptive extended Kalman filter convergence for a range of initial state model covariance values (Q_0), constant measurement covariance of $R = 4{-}7 \times I_4$, and a state model covariance gain of $M = 2$. The heating source is located at ($x = 2cm$, $y = 0cm$) with an initial guess of ($x = 0cm$, $y = 0cm$).

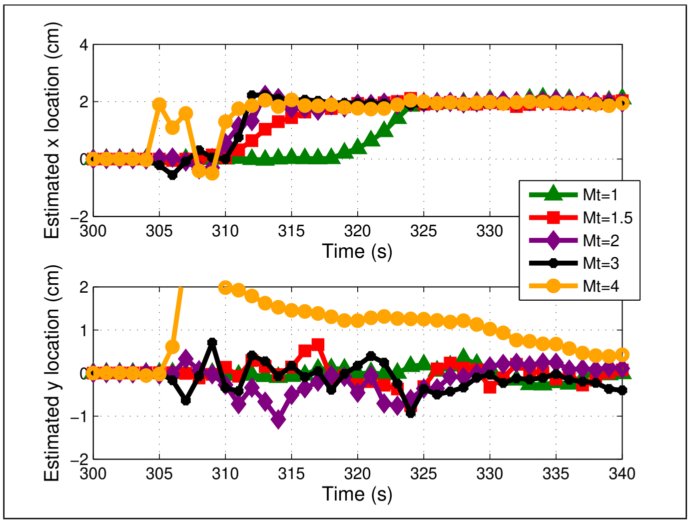

Figure 58: Adaptive extended Kalman filter convergence for a range of state model covariance gain values M, an initial state model covariance of $Q_0 = 1{-}4m^2 \times I_2$, and constant measurement covariance of $R = 4{-}7 \times I_4$. The heating source is located at ($x = 2cm$, $y = 0cm$) with an initial guess of ($x = 0cm$, $y = 0cm$).

7 Chapter Summary

This Chapter presents some fundamental concepts for detection, localization, and parameter estimation using inverse methods. These techniques can be used to characterize singularities, discontinuities, material properties, boundary conditions, loading, damage, structural changes, etc. Parameter estimation addresses the problem of estimating quantities that are not directly observable but that can be inferred from sensor data. Sensors carry only partial information and their measurements are corrupted by noise. Parameter estimation seeks to recover state variables from the sensor data using an iterative approach that incorporates a direct model.

References

M. Arulampalam, S. Maskell, N. Gordon, and T. Clapp. A tutorial on particle filters for online nonlinear/non-gaussian bayesian tracking. *IEEE transactions on signal processing*, 50(2):174–188, 2002.

J. Beck and K. Woodbury. Inverse problems and parameter estimation: integration of measurements and analysis. *Measurement Science and Technology*, 9:839–847, Jun 1998. doi: 10.1088/0957-0233/9/6/001.

J. V. Beck and K. J. Arnold. *Parameter Estimation in Engineering and Science*. John Wiley & Sons, 1977.

K. Berger, S. Rufer, R. Kimmel, and D. Adamczak. Aerothermodynamic characteristics of boundary layer transition and trip effectiveness of the HIFiRE flight 5 vehicle. In *AIAA Proceedings*, number AIAA-2009-4055, June 2009.

C. A. Brebbia and J. Dominguez. *Boundary elements: an introductory course*. WIT press, 1994.

O. Bretscher. *Linear Algebra With Applications*. Prentice Hall, 1995.

A. Doucet, N. Gordon, and V. Krishnamurthy. Particle filters for state estimation of jump Markov linear systems. *IEEE Transactions on Signal Processing*, 49(3):613–624, 2002.

K. J. Dowding and B. F. Blackwell. Sensitivity analysis for nonlinear heat conduction. *Journal of Heat Transfer*, 123(1):1, Feb 2001. doi: 10.1115/1.1332780.

M. Engelhardt, G. E. Stavroulakis, and H. Antes. Crack and flaw identification in elastodynamics using kalman filter techniques. *Computational Mechanics*, 37(3):249–265, 2006.

T. J. Horvath, S. A. Berry, and B. R. Hollis. Boundary layer transition on slender cones in conventional and low disturbance Mach 6 wind tunnels. In *32nd AIAA Fluid Dynamics Conference and Exhibit*, number AIAA-2002-2743, St. Louis, MO, 24–27 Jun 2002. AIAA.

F. P. Incropera and D. P. DeWitt. *Introduction to Heat Transfer*. John Wiley and Sons, Hoboken, NJ, 4th edition, 2002.

V. Kozlov, V. Adamchik, and V. Lipovtsev. Local heating of an unbounded orthotropic plate through a circular and annular domain. *Journal of Engineering Physics and Thermophysics*, 57:1381–1391, Jan 1989. doi: 10.1007/BF00871278.

P. d. S. Lopes, A. B. Jorge, and S. S. Cunha Jr. Detection of holes in a plate using global optimization and parameter identification techniques. *Inverse Problems in Science and Engineering*, 18(4):439–463, 2010.

M. Myers, A. Jorge, D. Yuhas, and D. Walker. An adaptive extended Kalman filter incorporating state model uncertainty for localizing a high heat flux spot source using an ultrasonic sensor array. *CMES: Computer Modeling in Engineering & Sciences*, 83(3):221–248, 2012a. doi: 10.3970/cmes.2012.083.221.

M. R. Myers, D. G. Walker, D. E. Yuhas, and M. J. Mutton. Heat flux determination from ultrasonic pulse measurements. In *International Mechanical Engineering Congress and Exposition*, number IMECE2008-69054. ASME, 2–6 Nov 2008.

M. R. Myers, A. B. Jorge, D. G. Walker, and M. J. Mutton. A comparison of extended Kalman filter, extended information filter, and least squares approaches for parameter identification of a transient heat transfer problem. In *Inverse Problems Symposium*, East Lansing, MI, 6–8 Jun 2010a. Michigan State University.

M. R. Myers, A. B. Jorge, D. G. Walker, and M. J. Mutton. A comparison of extended Kalman filter approaches using non-linear temperature and ultrasound time-of-flight measurement models for heating source localization of a transient heat transfer problem. In *Inverse Problems, Design and Optimization Symposium*, number IPDO-027, Brazil, 25–27 Aug 2010b. IPDO.

M. R. Myers, A. B. Jorge, M. J. Mutton, and D. G. Walker. High heat flux point source sensitivity and localization analysis for an ultrasonic sensor array. *International Journal of Heat and Mass Transfer*, 55 (9-10):2472–2485, Apr. 2012b. doi: 10.1016/j.ijheatmasstransfer.2012.01.012.

M. R. Myers, A. B. Jorge, M. J. Mutton, and D. G. Walker. A comparison of extended Kalman filter ultrasound time-of-flight measurement models for heating source localization. *Inverse Problems in Science and Engineering*, 20(7):991–1016, 2012c. doi: 10.1080/17415977.2012.669272.

M. R. Myers, D. G. Walker, D. E. Yuhas, and M. J. Mutton. Heat flux determination from ultrasonic pulse measurements. *International Journal of Heat and Mass Transfer*, in review, 2010. (in review).

Recreational Aviation Australia. Flow regimes. http://www.auf.asn.au, 2010. [Online; accessed 10-March-2010].

H. L. Reed, R. Kimmel, S. Schneider, D. Arnal, and W. Saric. Drag prediction and transition in hypersonic flow. In *AGARD CONFERENCE PROCEEDINGS AGARD CP*, volume 3, pages C15–C15. AGARD, 1997.

D. Salmond, N. Gordon, and A. Smith. Novel approach to nonlinear/non-Gaussian Bayesian state estimation. *IEE Proceedings-F, Radar and signal processing*, 140(2):107–113, 1993.

S. Schneider. Flight data for boundary-layer transition at hypersonic and supersonic speeds. *Journal of Spacecraft and Rockets*, 36(1):8–20, 1999.

S. Schneider. Hypersonic laminar-turbulent transition on circular cones and scramjet forebodies. *Progress in Aerospace Sciences*, 40(1-2):1–50, 2004. doi: 10.1016/j.paerosci.2003.11.001.

G. Stavroulakis and H. Antes. Flaw identification in elastomechanics: Bem simulation with local and genetic optimization. *Structural optimization*, 16(2):162–175, 1998.

S. Thrun, W. Burgard, and D. Fox. *Probabilistic Robotics*. The MIT Press, Cambridge, MA, 2006.

F. Vianna, H. Orlande, and G. Dulikravich. Prediction of the temperature field in pipelines with Bayesian filters and non-intrusive measurements. In *Proceedings of the 20th International Congress of Mechanical Engineering*, Gramado, RS, Brazil, 2009.

F. L. V. Vianna, H. Orlande, and G. Dulikravich. Temperature field prediction of a multilayered composite pipeline based on the particle filter method. *Proceedings of the 14th International Heat Transfer Conference*, 2010.

B. Vieira, A. Jorge, P. Lopes, and S. Cunha Junior. A Kalman filter model for an inverse problem of localization and identification of damage parameters on a 2-D structure. In *XXXII Cilamce-Iberian Latin-American Congress on Computational Methods in Engineering*, pages 1–18, 2011.

K. A. Woodbury, editor. *Inverse Engineering Handbook*. CRC Press, Boca Raton, FL, 2003a.

K. A. Woodbury. Sequential function specification method using future times for function estimation. In K. A. Woodbury, editor, *Inverse Engineering Handbook*. CRC Press, Boca Raton, FL, 2003b.

Annex: On the use of a Kalman Filter model for an inverse problem of localization and identification of damage parameters on a 2-D structure

An alternative to the finite element method detailed above, the boundary element method presents another tool for the direct model. In this annex, the boundary element method is used with a potential formulation and an elastostatic formulation for a plate with an inner hole representing damage to the plate. The damage here is treated as a circular hole, a geometric discontinuity, where the state, coordinates, and radius of the hole do not change with time, there is no control on the model, and the noise is considered to be white noise and low in amplitude.

Potential formulation

In the potential model, the plate and the hole are divided equally where its nodes should contain information on the x and y-directions on the temperature T and heat flux q. The number of elements that divide the plate and the number of elements that divide the hole need not be the same as this amount is the user's discretion, noting that the greater the division will produce more accurate results while also increasing computational cost.

This model consists of a temperature distribution on the surface of a square plate, six centimeters on each side. A temperature differential of 300 °C is applied between two edges with the other two edges and the hole adiabatic (i.e. the heat flow is zero). The potential model of the plate is illustrated by Figure 59.

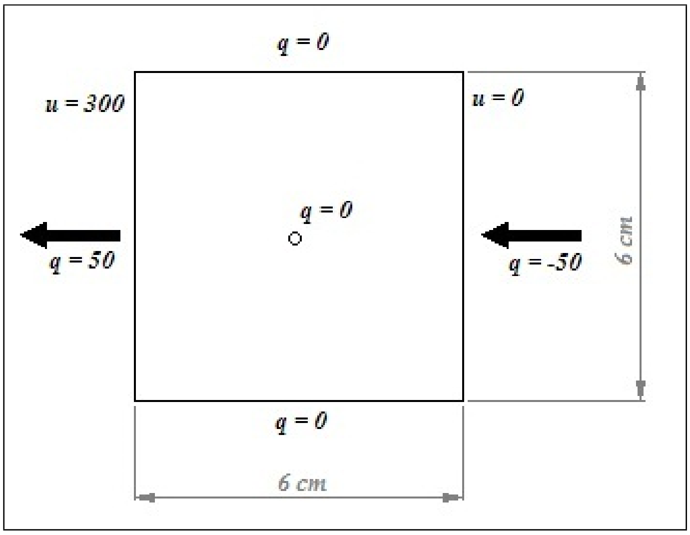

Figure 59: Plate model for the potential problem.

A hole of 0.06 cm of radius in the plate's center and the sensors were placed initially at 0.6 cm from the edges of the plate with a total of eight sensors. This sensor positioning was adopted, imagining a better utilization coupled with the possibility of easy positioning of thermocouples in the coordinates. With respect to the model developed in the boundary element method, the plate is divided into 12 elements and the hole with 24 elements, this division can be seen in Figure 60 along with the sensor positions.

Elastostatic formulation

As in the potential model, the plate and the hole are divided by elements, where its nodes should contain information on the x and y-directions, but now about the stress, shear τ or normal σ, or displacement δ prescribed itself. These stresses, normal and shear, cannot be used as a response of boundary element method in a damage detection problem, since they depend on the coordinate system used, or the normal direction of the cut plane that passes through the point of interest Lopes et al. [2010]. Therefore, it is necessary to use invariants of stress, which may be the average normal stress or octahedral stress.

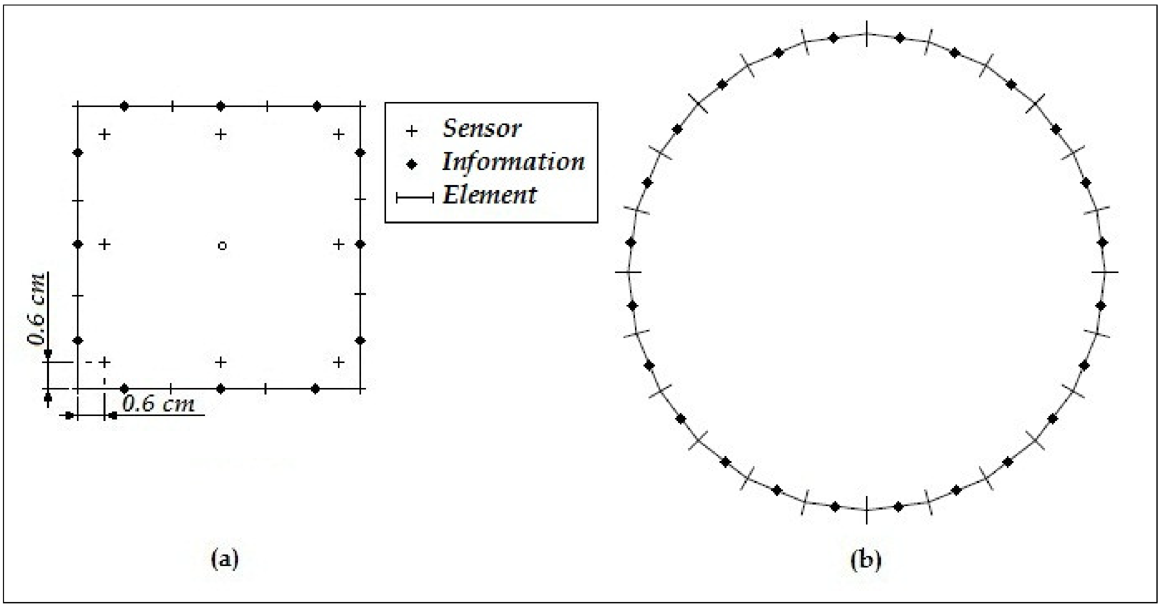

Figure 60: Potential model: (a) discretization of the plate and positioning of sensors, (b) discretization of the hole.

The average stress for the two-dimensional case is defined as:

$$\sigma_m = \frac{\sigma_x + \sigma_y}{2} \tag{68}$$

where σ_x is the normal stress in the axis direction x; σ_y is the normal stress in the axis y; and the octahedral stress, also in the two-dimensional case, is defined as:

$$\tau_{oct} = \sqrt{\frac{2}{9}\left[(\sigma_x + \sigma_y)^2 - 3(\sigma_x\sigma_y - \tau_{xy}^2)\right]} \tag{69}$$

The elastostatic model, consists of a plate of same dimensions as above with an applied load of 1,000 MPa traction on the plate towards the ordinate axis and leaving the other sides free. With respect to the hole, it is considered that there is no load. Figure 61 illustrates the model.

With respect to material of the plate, this is simulated considering a shear modulus of 94.5 GPa and a Poisson's ratio for plane strain of 0.1 Brebbia and Dominguez [1994], Lopes et al. [2010]. In this model, the hole used has a radius of 0.12 cm and sensors are positioned at 0.6 cm from the edges of the plate with a total of eight sensors. The plate is divided into 24 elements and the hole into 12 elements. The model is illustrated in Figure 62.

Potential model results

First the parameters were adjusted for the direct and inverse problem, where most parameters are determined by trial and error. Soon, after a few iterations, the following parameters were adopted:

$$R = \left(\frac{0.01 I_{8x8}}{3}\right)^2, \tag{70}$$

$$Q = \begin{bmatrix} 0.1 & 0 & 0 \\ 0 & 0.1 & 0 \\ 0 & 0 & 0.01 \end{bmatrix}^2, \tag{71}$$

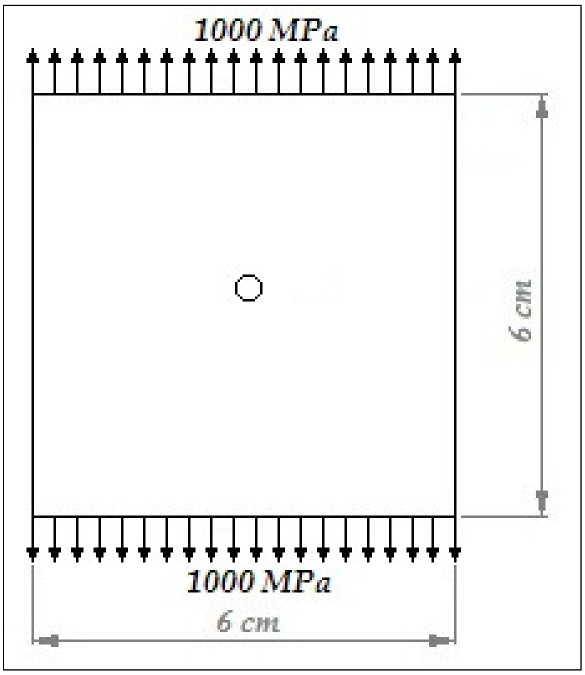

Figure 61: Plate model for the elastostatic problem.

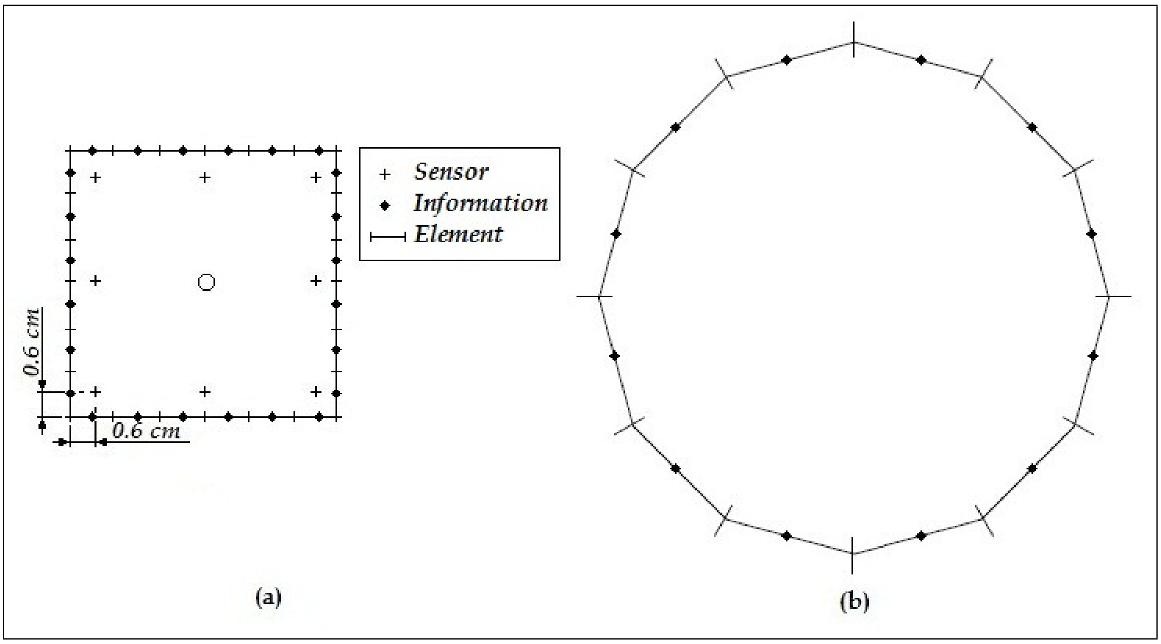

Figure 62: Elastostatic model: (a) discretization of the plate and positioning of sensors, (b) discretization of the hole.

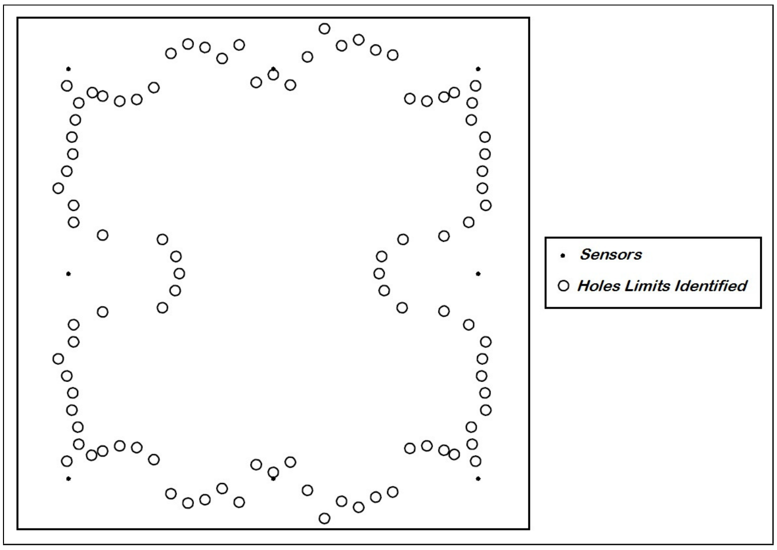

Figure 63: Region limit of identification of the filter for the sensor to 0.6 cm from the edges of a plate of 6x6 cm.

and the variations of the components of the state to calculate the sensitivity matrix

$$\Delta_x = \Delta_y = \Delta_r = 0.002 \tag{72}$$

The covariance matrix of the measurement noise was defined as the accuracy of a thermocouple of 0.01 °C, multiplied by the identity (each sensor has no effect on the other and they are not correlated). The covariance of the noise process, which also is not correlated, provides values only on the main diagonal, and the noise values being 10% and 1% of the state, to the coordinates and size of the hole, respectively.

With these parameters, using sensors at a distance of 0.6 cm from the edges and a maximum of 50 iterations, the Kalman filter obtained a result with error less than 0.3% for any of the three components of the state within a region that is illustrated by Figure 63, whose area is 20.56 mm^2.

When positioning the hole outside the region, which is 0.1 mm displacement, the error for the estimation of the filter jumps to extremely high values. This setting limit shows that the boundary conditions, as well as the sensors, interfere with the results of the estimation of the filter. The position of the sensors, therefore, is limited to a distance of 0.06 cm from the plate edges. The acceptable sensor region is illustrated in Figure 64 whose area is 21.48 mm^2 and the errors are less than 0.05%.

For this model, with these settings used, the positioning of sensors interferes in performance of the Kalman filter. For both configurations, the positioning of sensors has an increase of 4.47% of the area detectable by the Kalman filter. This inner region is where the filter locates and identifies the hole, since the external region have points that the filter can locate and identify, but randomly, being some isolated points and other forming small sub-regions.

For the positioning sensor to 0.06 cm from the edges, for a hole with coordinates (2.00;2.00) cm and radius equal to 0.06 cm, the Kalman filter produced results presented in Figures 65-68.

Elastostatic model

Figure 69 shows the results of the Kalman filter for the elastostatic model using as parameters:

$$Q = \left(\begin{bmatrix} 0.1 & 0 & 0 \\ 0 & 0.03 & 0 \\ 0 & 0 & 0.001 \end{bmatrix} * 10^3 \right)^2, \tag{73}$$

$$R = (\sigma_{z_k} I_{8x8})^2, \Delta_x = \Delta_y = 0.00035, \tag{74}$$

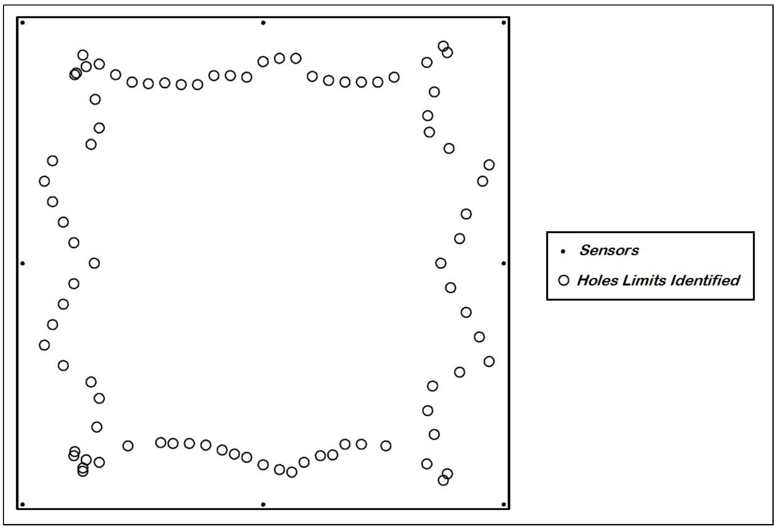

Figure 64: Region limit of identification of the filter for the sensor to 0.6 cm from the edges of a plate of 6x6 cm.

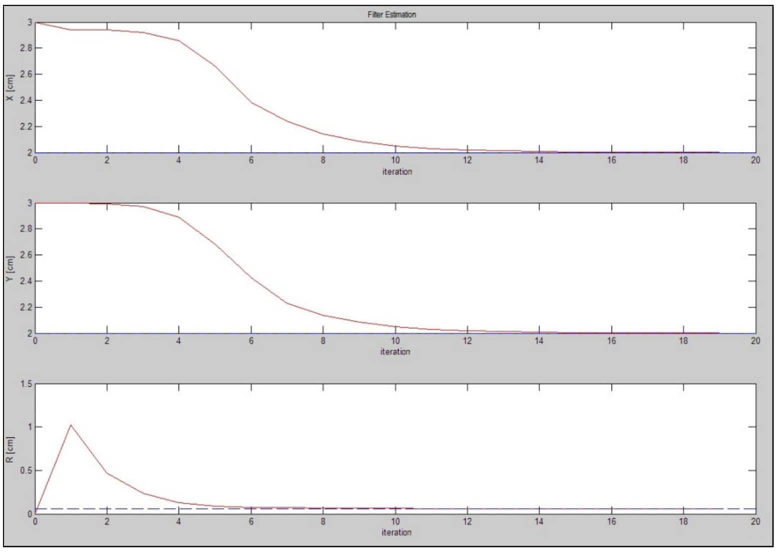

Figure 65: Estimation of components of state for a hole (2.00;2.00;0.06) cm for a potential model.

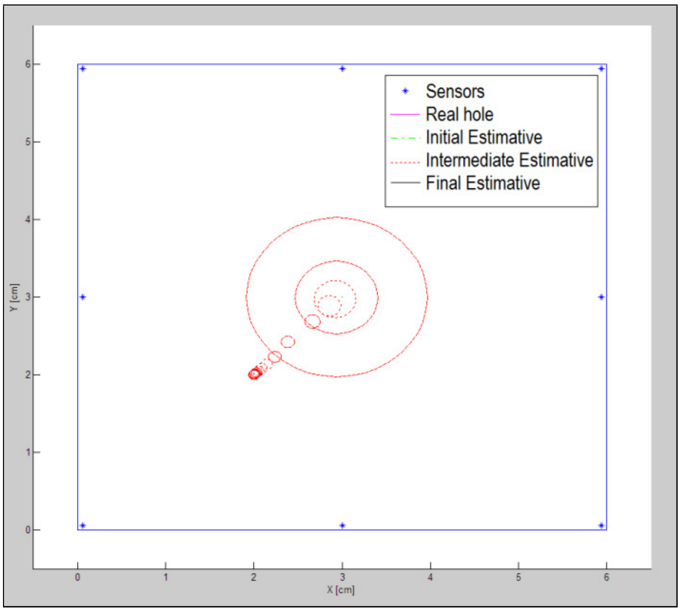

Figure 66: Performance of Kalman filter for a hole (2.00;2.00;0.06) cm for a potential model.

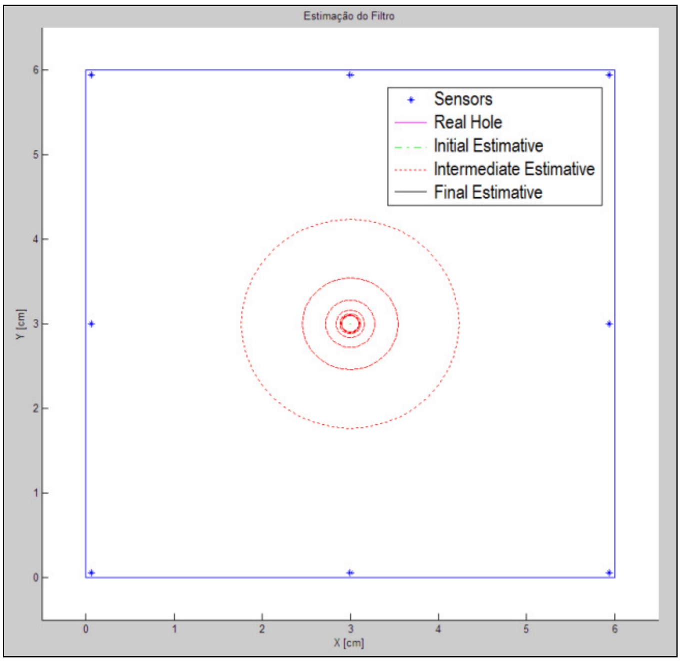

Figure 67: Performance of Kalman filter for a hole (3.00;2.00;0.06) cm for a potential model.

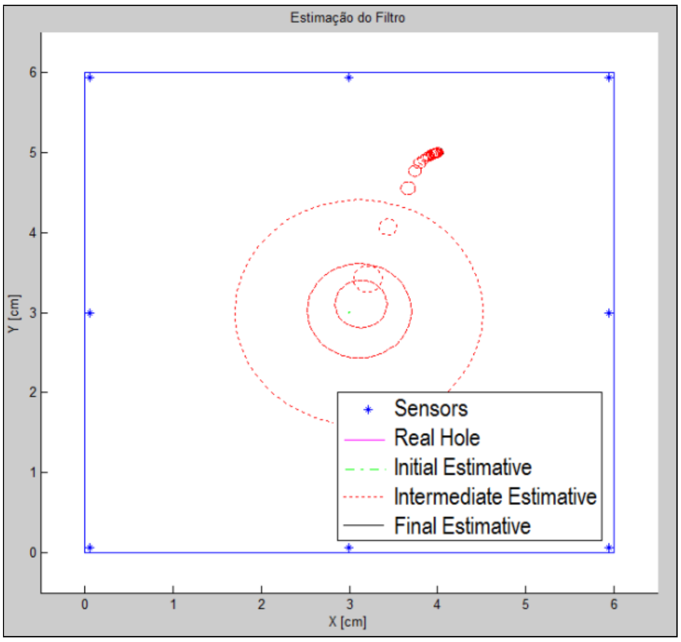

Figure 68: Performance of Kalman filter for a hole (4.00;5.00;0.06) cm for a potential model.

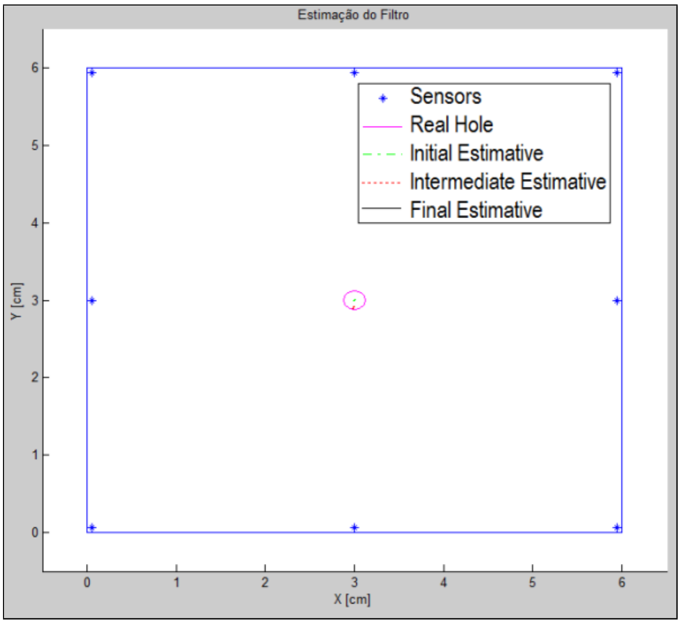

Figure 69: Performance of Kalman filter for a hole (3.00;3.00;0.06) cm for an elastostatic model.

and

$$\Delta_r = 0.002 \tag{75}$$

The tolerance for conversion is 1 x 10^{-3} and the maximum number of iterations equal to 75. In the measurement noise the covariance consists of the standard deviation of measured (σ_{z_k}) times the identity matrix (I_{8x8}).

Summary

In this annex, an inverse problem using the Kalman filter has been presented for localization and identification of damage parameters with a potential and an elastostatic formulation of a 2-D problem. A hybrid model of was presented where the state is described by a linear model and the measurements by a non-linear model, obtained from the numeric results of a boundary element method model of the direct problem.

In both formulations, the local information is obtained at an interior point (the temperature, for the potential case and the average stress or the octahedral stress for the elastostatics case), is a scalar quantity, and thus it is not dependent on the coordinate system. For the potential formulation with an adequate positioning of the sensors, there was an interior region in the domain in which the Kalman filter was able to identify and locate the hole. For the elastostatic formulation, the number and location of the internal points must be optimized to properly locate and identify the presence of the hole.